Extreme events over the contiguous United States portrayed in a CESM-WRF dynamical downscaling framework

By

Lei Cai

Submitted to the Department of Geography and the
Graduate Faculty of the University of Kansas
in partial fulfillment of the requirements for the degree of
Master of Science

David B. Mechem, Chairperson

Committee members

Nathaniel A. Brunsell

Bryan C. Young

Date defended: 07/25/2014

The Thesis Committee for Lei Cai certifies
that this is the approved version of the following thesis :

Extreme events over the contiguous United States portrayed in a CESM-WRF dynamical downscaling framework

David B. Mechem, Chairperson

Date approved: 09/08/2014

Abstract

A dynamical downscaling framework is adopted to explore historical (1950-1999) and projected (2050-2099) behavior of extreme precipitation (PR), maximum temperature (TMAX) and minimum temperature (TMIN) events within the contiguous United States. Compared to reanalysis data, simulations represent temperature better than precipitation, and the model performs better east of the Rocky Mountains than over the mountainous west. Extreme events are defined according to exceedances of percentiles of the distribution of precipitation and temperature variables (typically the 90^{th}, 95^{th}, and 99^{th} percentiles), as well as the actual magnitudes corresponding to the percentiles. After applying a bias-correction to all three variables, extreme percentile thresholds show broadly higher values for all three variables in the projected simulation compared to the historical simulation. Precipitation extremes show no systematic trends of frequency or intensity in either the historical or the projected simulations. Trends of TMAX and TMIN have frequency and intensity that are consistently positive in the historical simulation, but the positive trend patterns are somewhat different in the projected simulation. In the projected simulation, all climate zones exhibit consistent increases in PR and TMAX extremes, and a decrease in TMIN extremes, both in the frequency and intensity. Northern zones such as Dfa and Dfb exhibit more changes of extremes in the projected simulation compared to other zones. On the other hand, the patterns of extreme frequency and intensity in all zones suggest their dependence on regional climatologies (e.g., B class zones have more frequent TMAX and less frequent PR than other zones, while D class zones have lower TMAX and TMIN intensity than other zones). In the projected simulation, PR intensity increases more

significantly than frequency, while frequency increases more than intensity for TMAX and TMIN. The projected heat waves (defined as high temperature events lasting multiple days) are more severe in both number and duration, which results predominately from the increasing of the mean TMAX.

Acknowledgements

This thesis would not be possible without the funding provided by U.S. Department of Energy (DOE), grant DE-SC0005359, and National Science Foundation EPSCoR program, grant EPS-0553722 and EPS-0919443. I would like to thank my graduate adviser, David B. Mechem, for his great support and encouragement to my study and live in a foreign country, and to my committee members, Nathaniel A. Brunsell and Bryan C. Young, for their valuable ideas in putting thesis thesis all together. I also wish to thank our collaborator, Andrew Monaghan from NCAR, for tireless grateful help in making available this preprocessing code and establishing the computational environment on the Bluefire and Yellowstone. At last, I wish to thank my family and friends, as well as my fiancee, Yu Lian, for their warm-hearted help and encouragement during the last three years.

Contents

1 Introduction **1**

2 Data Source **4**

2.1 Overview 4

2.2 Community earth system model version 1 4

2.3 Weather research and forecasting model 5

2.4 North American regional reanalysis data 7

3 Methodology **8**

3.1 Definition of extreme events 8

3.2 Model evaluation 9

3.3 Bias correction 12

3.4 Köppen-Geiger Classification 13

4 Results **15**

4.1 Percentile thresholds and their differences 15

4.2 Change of extremes through time 18

4.2.1 Trends in the historical simulation 19

4.2.2 Trends in the projected simulation 23

4.2.3 Comparison of the historical and projected trends 31

4.3 Extremes in Köppen-Geiger climate zones 31

4.4 Quantification of heat waves in terms of Köppen-Geiger climate zones 38
4.5 Origin of more extreme TMAX events and more severe heat waves 42

5 Discussion **46**

6 Conclusion and future work **50**

List of Figures

2.1 The simulation region for WRF, outlined by the red box. 6

3.1 (a), (b), (c) show difference between WRF and NARR (WRF minus NARR); (d), (e), (f) show difference between CESM and NARR (CESM minus NARR); (g), (h), (i) show difference between WRF and CESM (WRF minus CESM). 10

3.2 Chosen climate zones over contiguous United States based on Köppen-Geiger classification. 14

4.1 Historical extreme values corresponding to the 90^{th}, 95^{th}, and 99^{th} percentile of distribution for PR (left panel), and TMAX (middle panel), and to the 1^{st}, 5^{th}, and 10^{th} percentile of distribution for TMIN (right panel). 16

4.2 As Fig. 4.1, but for the projected simulation. 17

4.3 Differences between projected and historical extreme values corresponding to the 90^{th}, 95^{th}, and 99^{th} percentile of distribution for PR (left panel), and TMAX (middle panel), and to the 1^{st}, 5^{th}, and 10^{th} percentile of distribution for TMIN (right panel). 18

4.4 Contour maps of the frequency trend of PR, TMAX, and TMIN extremes (left panel), as well as the corresponding intensity trend (right panel) in the historical simulation. Dotted regions outlined by red contour lines are tested significant for positive trend, and regions outlined by black contour lines test significant for negative trend. 21

4.5 Contour maps of the frequency trend of PR in four seasons, as well as the corresponding intensity trend (right panel) in the historical simulation. Dotted regions outlined by red contour lines are tested significant for positive trend, and regions outlined by black contour lines test significant for negative trend. 22
4.6 As in Fig. 4.5, but for TMAX. 24
4.7 As in Fig. 4.5, but for TMIN. 25
4.8 As in Fig. 4.4 but for the projected simulation. 27
4.9 Contour maps of the frequency trend of PR in four seasons, as well as the corresponding intensity trend (right panel) in the projected simulation. Dotted regions outlined by red contour lines are tested significant for positive trend, and regions outlined by black contour lines test significant for negative trend. 28
4.10 As in Fig. 4.9, but for TMAX. 29
4.11 As in Fig. 4.9, but for TMIN. 30
4.12 Box plots for frequency (a) and intensity (b) of extreme precipitation in spring. Within each climate zone, the red box denotes the historical simulation and the blue box denotes the projected simulation. Colored dots indicate the difference between the two samples in that climate zone is statistically significant. 33
4.13 Same as Fig. 4.12 except for the season of summer. 34
4.14 Same as Fig. 4.12 except for the season of fall. 35
4.15 Same as Fig. 4.12 except for the season of winter. 35
4.16 Box plots for frequency (a) and intensity (b) of TMAX in summer. Within each climate zone, the red box denotes the historical simulation and the blue box denotes the projected simulation. Colored dots indicate the difference between the two samples in that climate zone is statistically significant. 37
4.17 Same as Fig. 4.16 except for TMIN in winter. 37

4.18 Box plots for downscaled mean duration of heat waves (a) and mean number of heat waves per year (b). Red boxes correspond to the historical heat waves, and blue boxes to the projected heat waves calculated from 20^{th} century thresholds, T1 and T2. Purple boxes are for projected heat waves from thresholds T1′ and T2′. . . 40

4.19 Same as Fig. 4.18 except for data from CESM. 41

4.20 (a): Violin plots of TMAX distribution for each climate zone in both the historical (red) and projected (blue) simulation. (b): TMAX increases in the projected simulation compared to the historical simulation of 81^{st} (red), 90^{th} (blue), and 97.5^{th} (green) percentile values, as well as the mean (black) for every climate zones. . . . 44

5.1 Mean annual precipitation (mm) from 1950-1960 from output of the upgraded version of historical downscaling simulation. 48

List of Tables

2.1 Parameterization schemes chosen for model initialization 6

3.1 Climatology for each Köppen-Geiger climate zone 14

4.1 Percentile values and mean difference between projected and historical simulation (projected minus historical) 43

Chapter 1

Introduction

Compared to climatological studies that have primarily focused on the evolution of mean conditions of precipitation and temperature, interest in studying climatic extremes has only come about over the last 20 years (Easterling et al., 2000a). However, people have gradually accepted that even short-term extreme climatic events can cause substantial problems to society. For example, heat waves and drought struck the United States in the summer of 2012, the third warmest summer on record, and caused severe losses to agriculture, economy, and human health (`http://www.ncdc.noaa.gov/news/summer-2012-drought-update`). Observational data exhibits an increasing trend of extreme temperature and precipitation events since the year 1850 (Kunkel et al., 2003; Alexander et al., 2006; Solomon et al., 2007), and the increases have been accelerating since the mid-1970s (Kunkel et al., 2003). The spatial distributions and temporal trends of extreme events, as well as their potential causes, therefore constitute a critical topic to study.

Previous studies exploring extreme events have been predominately observational. Multi-decadal observational data from weather stations indicated that the number of heavy precipitation events increased globally over the 20^{th} century, no matter whether the annual mean precipitation amount over those regions increased or decreased (Alexander et al., 2006; Groisman et al., 2001), and the increasing precipitation extremes in the second half of 20^{th} century are largely manifested as the amplified tail of precipitation distribution (Easterling et al., 2000a). Furthermore, the fre-

quency and intensity of extreme events over the contiguous United States has also become greater over the last 64 years (Higgins et al., 2011).

Episodes of extreme events lasting for multiple consecutive days cause serious impacts, including heat and cold waves, flooding, and drought. One observational study found an increase in heat waves and a decrease in cold waves over U.S. since 1950, though exceptions occur over relatively small regions (Peterson et al., 2013). Droughts and flooding, which are precipitation-related events, do not show any uniform changes through time (Peterson et al., 2013).

Since observations by nature address only historical events, numerical modeling thus becomes an obvious approach for exploring projected extreme events in the future. Modeling studies have been exploring extremes since the late 20^{th} century when various highly advanced global models were established. The Coupled Model Intercomparison Project phase 5 (CMIP5) (Taylor et al., 2012) is the latest phase of CMIP, and includes global climate projections from multiple advanced atmosphere-ocean global climate model (AOGCM) simulation products under varied forcing scenarios. One study based on CMIP5 ensembles found increases of extreme precipitation and temperature events in both historical simulations and future projections, although the magnitudes of increases vary from model to model (Wuebbles et al., 2014).

Limited by computational expense considerations, long-term GCM (Global Climate Model) simulations at present are practical only for minimum grid spacings of about 1 degree and are not capable of fully capturing mesoscale systems like storms and heavy rainfall. Dynamical downscaling, forcing a regional model using GCM output over a limited-area domain, is one pathway for improving the representation of local meteorological phenomena. This downscaling approach yields model output with both small grid spacing and long temporal coverage. Bell et al. (2004) performed dynamical downscaling using the CCM3 (Community Climate Model version 3) to drive the RegCM2 (Regional Climate Molde version 2) to explore both historical and projected heavy rain and high temperature events in the State of California. CCM3-RegCM2 projected future changes in climatic variables, and found that regions with complex topography and land use gradients benefited from the high-resolution grid and detailed representation of atmospheric pro-

cesses that only the RCM could provide. Downscaled output described better extreme precipitation and temperature events in study area compared with those in GCM.

The North American Regional Climate Change Assessment Program (NARCCAP) (Mearns et al., 2012b) is an international program that includes a number of GCM-RCM downscaling combinations for exploring detailed historical and projected climate change over North America. Output from the NARCCAP simulations represent better than the GCM convective processes over terrains with complex topography like the California coastal region, thus more accurately reproducing extreme precipitation behavior (Gutowski et al., 2010). In particular, the tails of the precipitation distributions from the NARCCAP simulations agree well with observational data, suggesting the NARCCAP simulations perform reasonably in representing extreme precipitation behavior (Weller et al., 2013). Two shortcomings of NARCCAP are that the GCMs employed in NARCCAP are mostly from the previous generation CMIP3 participating models, and that the only GCM simulations chosen are from the most extreme emission scenario (A2) (Nakicenovic et al., 2000).

Summarizing the previous research in this field strengthens the essentiality of studying extreme events over the contiguous United States, and exploring future projections of extremes necessitates a downscaling modeling approach. This research addresses two questions: (1) What insights into the spatial distributions and temporal trends of extreme behaviors of regional climate are provided from dynamical downscaling? (2) What's the dependence of these extreme statistics on climate zone?

These two research questions lead to the following hypotheses:

Hypothesis 1: Assuming the dynamical downscaling approach reproduces reasonable precipitation and temperature fields, extreme precipitation and maximum temperature events will be more frequent and exhibit greater magnitudes in the projected simulation relative to the historical simulation, while extreme minimum temperature events will be less common and less intense (warmer).

Hypothesis 2: Statistics of extreme events will vary by zone, with the northern U.S. east of the Rocky Mountains exhibiting the greatest increase in extremes in a projected climate.

Chapter 2

Data Source

2.1 Overview

This research employs a regional dynamical downscaling framework in which the Weather Research and Forecasting model (WRF) (Skamarock et al., 2005) is forced by the Community Earth System Model version 1 (CESM1) (Gent et al., 2011). North American Regional Reanalysis (NARR) (Mesinger et al., 2006) data is used as the reference for model evaluation and as a basis for bias-correcting the climatic variables .

2.2 Community earth system model version 1

This research employs CESM1 output to formulate initial and boundary conditions for the RCM (WRF in this study). CESM1 was first released on April 2010 as one of the CMIP5 participating models (Taylor et al., 2012). The "20^{th} Century Ensemble Member #6" simulation is the forcing for the historical simulation, and the "RCP6.0 Ensemble Member #6" simulation is the forcing for the projected simulation. RCP6.0, which is short for "Representative Concentration Pathway 6.0", assumes a rising CO_2 concentration in the 21^{st} century producing an increase in radiative forcing of 6.0 Wm^{-2}. These two simulations are the only members for which 6-hourly output is available online, which satisfies the WRF initialization requirement for this research.

2.3 Weather research and forecasting model

WRF is designed to be a flexible, state-of-the-art atmospheric simulation system that is efficient on parallel computing platforms. It provides various physical parameterization schemes for boundary layer dynamics, microphysics, convection, and longwave/shortwave radiations, enabling simulations across different scales (Skamarock et al., 2005). As previously discussed, WRF has been used in a wide array of downscaling applications. Bukovsky and Karoly (2009) applied WRF in a dynamical downscaling framework within the contiguous United States, finding an appropriate combination of parameterization schemes to reproduce as accurately as possible the precipitation field over the U.S.

We run WRF (verison 3.3) over the periods 1950-1999 (historical simulation) and 2050-2099 (projected simulation). The domain has 200×150 grid points with a horizontal grid spacing of 30 km, which includes the contiguous United States as well as part of Canada and Mexico (Fig. 2.1). Our simulation specifies 27 vertical atmospheric levels and 4 soil layers. Various parameterization schemes are employed for different physical processes (Table. 2.1). For microphysical processes, the WRF single-moment 3-class scheme is chosen. The rapid radiation transfer model (RRTM) (Mlawer et al., 1997) and Dudhia scheme (Dudhia, 1996) are used for longwave and shortwave radiation, respectively. The Noah land surface model (Noilhan and Planton, 1989) is responsible for land surface processes, and the Yonsei University scheme (Hong and Dudhia, 2003) parameterizes planetary boundary layer dynamics. Simulations use the Kain-Fritsch convective parameterization (Kain, 2004). All schemes are listed in Table 2.1. This parameterization combination has also been proven to be well behaved for regional climate WRF simulations (Bukovsky and Karoly, 2009). A series of 1-year-period test simulations conducted prior to the long-term simulations found that more complex microphysical schemes like the WRF single-moment 5-class scheme overestimates the spatial variability in precipitation over the eastern U.S., whereas simpler parameterization like the Kessler scheme is not plausible since it only considers warm rain. The Betts-Miller-Janjic (BMJ) (Betts, 1986; Betts and Miller, 1986; Janjic, 1994) convective parameterization scheme underestimates precipitation over mountainous regions and produces too much precipitation over the

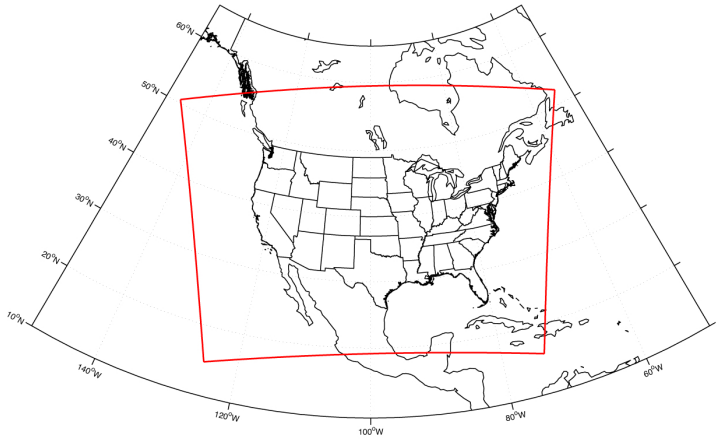

Figure 2.1: The simulation region for WRF, outlined by the red box.

southeast U.S. The zonal and meridional wind speeds (u and v), temperature (T), and water vapor mixing ratio (qvapor) above the 25^{th} vertical level (eta < 0.032) are nudged, which is above the pressure level of 32 mb. Nudging helps to constrain upper level modeling toward its forcing (GCM). The nudging coefficient is set to 0.0003 for all four variables, corresponding to a nudging time scale of about 3333 seconds.

Table 2.1: Parameterization schemes chosen for model initialization

Physics	Parameterization Scheme
Microphysics	Single-moment 3-class (WSM3)
Longwave Radiation	Rapid Radiation Transfer Model (RRTM)
Shortwave Radiation	Dudhia
Land Surface Processes	Noah Land Surface Scheme
Boundary Layer Dynamics	Yonsei University Scheme
Convection	Kain-Fritsch

2.4 North American regional reanalysis data

We employ North American Regional Reanalysis (NARR) (Mesinger et al., 2006) for model evaluation. Bukovsky and Karoly (2007) found that NARR represents precipitation behavior over the contiguous U.S. reasonably well. Compared to previous global reanalysis products, NARR exhibits an improved representation of land-atmosphere interactions by successfully assimilating high-quality precipitation and surface temperature observations (Becker et al., 2009; Mesinger et al., 2006). The grid spacing of NARR is 32 km, which is the finest reanalysis data-set available for the North American continent at present. The high quality of assimilated climatic variable fields and similar grid spacing to our WRF configuration both make NARR suitable for validating and correcting downscaling output for this study. In this research, 6-hourly precipitation and temperature fields from NARR are extracted from 1979 to 1999, the overlapping period of NARR and WRF historical simulation.

Chapter 3

Methodology

3.1 Definition of extreme events

Percentile thresholds, together with the frequency and intensity of extremes that are based on percentile thresholds, are employed to determine extreme events. We define extreme thresholds of daily precipitation (PR) and daily maximum temperature (TMAX) according to 90^{th}, 95^{th}, and 99^{th} percentile values of the PDFs (Probability Distribution Functions) of the corresponding variables. Extreme minimum temperature (TMIN) thresholds correspond to 10^{th}, 5^{th}, and 1^{st} percentile values of the TMIN PDFs. In this research, PDFs of PR, TMAX, and TMIN are constructed at every grid point over the whole simulation period, or for selected seasons.

The frequency of extreme events (either PR, TMAX, or TMIN) for year y is defined as the ratio of the number of events (number of days for the temperature extremes) that exceed the percentile threshold (90% extreme threshold) to the total number of events (number of days in a whole year for the temperature extremes), described according to the following equation. For precipitation, the frequency has the unit of events/day, and for TMAX and TMIN, their frequencies are with the unit of days/day.

$$F_y = \frac{N_{P>P^*}}{N_P}$$

The intensity of extreme events for the year y is defined as the sum of climatic variable values (precipitation and temperature) that lie above the percentile thresholds (or below the thresholds for TMIN) for that year divided by the number of the exceedances in that year, as in the following equation. Units are in mm for PR and K for TMAX and TMIN:

$$I_y = \frac{\sum_{i=1}^{n} P_{P>P^*}}{N_{P>P^*}}$$

Therefore, this equation defines the intensity of extremes as the mean magnitude of exceedance of 90% extreme threshold in that year.

3.2 Model evaluation

CESM-WRF outputs precipitation and temperature fields in a 6-hour time interval, at 0000, 0600, 1200, and 1800 UTC. The highest temperature among these four values each day is picked as TMAX, while the lowest temperature is picked as TMIN. This method of approximating TMAX and TMIN may introduce bias compared to observations or other model datasets in which the true TMAX and TMIN are calculated.

In our dynamical downscaling configuration, biases may arise from both the GCM and the RCM. Model evaluation therefore becomes especially important to establish the veracity of any dynamical downscaling approach. The evaluation of NARCCAP output compared mean precipitation and temperature fields between the model results and the reanalysis data sets in order to quantify simulation bias (Mearns et al., 2012a; Bukovsky et al., 2013). In this research, we evaluate the CESM-WRF downscaling approach by comparing long-term means of precipitation and temperature between every two members of these three data sets: WRF and CESM; WRF and NARR; NARR and CESM. Data from these three data sets are all chosen from the overlapping period of NARR and WRF, the years of 1979-1999. Fig. 3.1 presents the difference maps for PR, TMAX, and TMIN, between WRF and CESM (WRF minus CESM), CESM and NARR (CESM

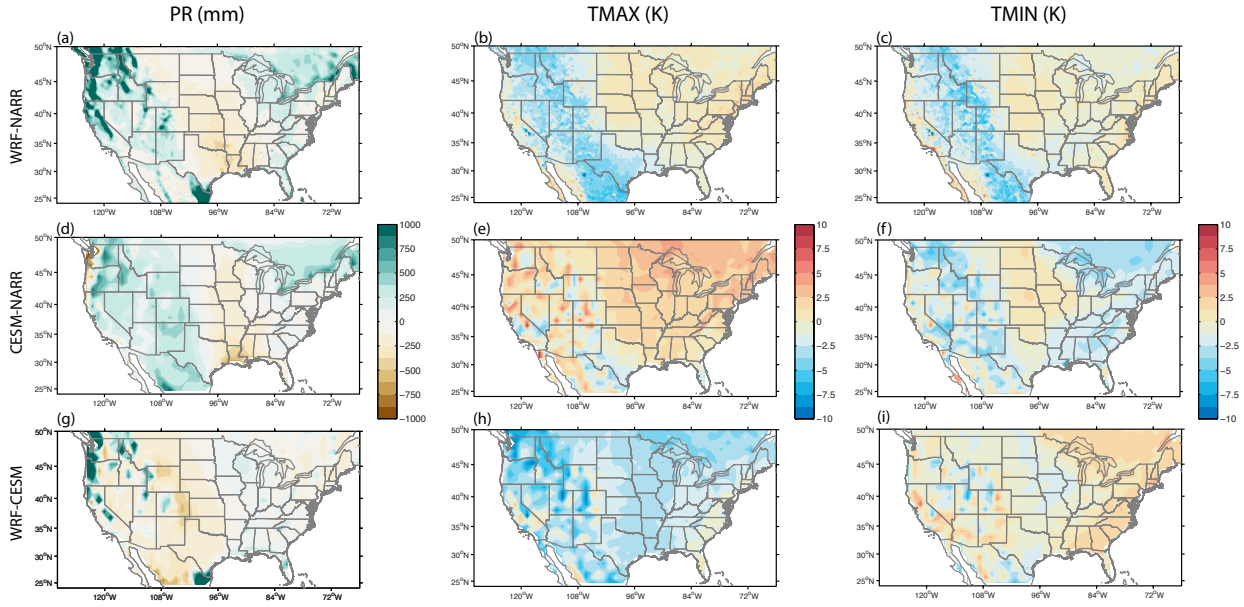

Figure 3.1: (a), (b), (c) show difference between WRF and NARR (WRF minus NARR); (d), (e), (f) show difference between CESM and NARR (CESM minus NARR); (g), (h), (i) show difference between WRF and CESM (WRF minus CESM).

minus NARR), as well as WRF and NARR (WRF minus NARR). This approach allows us to investigate the origin of the bias between CESM-WRF and the observational fields (as represented by NARR).

For precipitation, The region east of Mississippi River shows a good fit between WRF and NARR (< 125 mm annual difference). However, over the western mountainous U.S., WRF-NARR and CESM-NARR maps both show wet biases (Fig. 3.1a and Fig. 3.1d). Fig. 3.1g suggests that WRF contributes substantially to the wet bias over the high topography, and also appears to introduce a dry bias just downstream (east) of the mountain peaks. Dry biases found in both WRF-NARR and CESM-NARR map lie over the central U.S. The greatest dry bias is over the southern states adjacent to the Gulf of Mexico, and then decreases towards the north (Fig. 3.1d).

Relative to reanalysis, TMAX in the WRF simulation generally shows slight warm biases (<1 K) east of the Rocky Mountains, and about 3 K of cold biases over mountainous regions (Fig. 3.1b). CESM is systematically warmer over much of the domain (Fig. 3.1e), except in the mountain regions, which show a mix of warm and cold bias. Over the entire domain, TMAX in WRF is

systematically cooler compared to CESM (Fig. 3.1h). These temperature biases are in the 2∼5 K range, but as we discuss below, the difference in the way TMAX is calculated partially explains the behavior of the fields in Fig. 3.1.

TMIN shows similar WRF-NARR patterns, with warm bias less than 1 K over the central and eastern U.S., and around 3 K cold bias over western U.S. (Fig. 3.1c). CESM exhibits similar TMIN behavior (Fig. 3.1f), with slightly greater positive bias over the central U.S. (compared to the WRF-NARR differences) and weaker negative bias over the mountains. The difference between WRF and CESM for TMIN (Fig. 3.1i) are somewhat weaker and not systematically negative as they are for TMAX (Fig. 3.1h).

WRF represents the temperature field to the east of Rocky Mountains well, while TMAX and TMIN cold biases over western U.S. on may partially result from the cooling effect of excessive precipitation. On the other hand, temperature biases are higher in WRF-CESM and WRF-NARR comparisons. The difference in how TMAX and TMIN are calculated in the different datasets may have an important influence on model bias. Of the three datasets (CESM, WRF, and NARR), only CESM extracts the true daily maximum and minimum temperatures, while WRF and NARR estimate TMAX and TMIN based on 6-hourly output. For this reason, TMAX and TMIN obtained from WRF and NARR are generally ∼2-3 hours away from the time when the actual TMAX and TMIN occur each day This discrepancy may explain some portion of ∼2-5 K higher TMAX values for CESM compared to both WRF and NARR (which also explains why the WRF-CESM difference in Fig. 3.1h is negative). Since NARR's TMAX and TMIN are extracted as the same way as WRF's, the difference of TMAX and TMIN between these two data sets to the east of Rocky Mountains is generally less than 1 K (Fig. 3.1b-c). Over higher altitudes, WRF and CESM show slight cold biases for both TMAX and TMIN relative to NARR.

In summary, our downscaled simulations perform better on temperature than precipitation. Precipitation biases in WRF are particularly evident over regions of topography to the west of the Rocky Mountains, much greater than CESM-NARR precipitation biases over the same area. The dry biases over central U.S. including Gulf States appear to be related to the original GCM

forcing. Except for the cool bias over mountainous area, which we speculate is mostly due to the wet precipitation bias there, TMAX and TMIN in the WRF simulation (and in the CESM simulation, for that matter) generally compare favorably with the reanalysis. Before performing more in-depth analysis, we apply bias correction on the precipitation field. Although not strictly necessary, for consistency we also apply a bias correction to the TMAX and TMIN fields.

3.3 Bias correction

In this research, bias correction is conducted using the linear scaling method (Lenderink et al., 2007), which is relatively simple compared to other methods that rescale the whole distribution (Teutschbein and Seibert, 2012). Linear scaling rescales the distribution such that the long-term mean of simulated distribution and the mean of observed distribution are equal. This method artificially rescales modeled PDFs to fit the observational long-term means and keep the same probability densities of each percentile values as the uncorrected PDFs. The linear scaling method is applied for precipitation using the following formulas:

$$P^*_{his}(d) = P_{his}(d)\frac{\mu_m(P_{obs}(d))}{\mu_m(P_{his}(d))}$$

$$P^*_{prj}(d) = P_{prj}(d)\frac{\mu_m(P_{obs}(d))}{\mu_m(P_{his}(d))}$$

in which $P^*_{his}(d)$ and $P^*_{prj}(d)$ is the daily bias-corrected precipitation for the historical and projected simulations, $P_{his}(d)$ and $P_{prj}(d)$ are the original ones for those two simulations, $P_{obs}(d)$ is the daily precipitation from observational data (NARR in this case), and μ_m stands for the long-term mean precipitation.

In this research, long-term means of observed and modeled PR are calculated choosing the

overlapping period of NARR and WRF, the year 1979-1999. The NARR grid is interpolated onto the CESM-WRF grid points using the nearest-neighbor method. Distances from actual location of every grid point to their selected nearest neighbor points are all less than 3 km, which amounts to 10% of the horizontal grid spacing in WRF. Thus, any error arising from the interpolation method is small. Grid points with high bias ($> 40\%$) between the uncorrected WRF precipitation field and the NARR precipitation field are removed from the study area.

Since precipitation and temperature co-vary and are also spatially and temporally autocorrelated, accuracy of the temperature fields must be affected over grid points with high precipitation bias. Therefore, we eliminate 1% of the grid points within the entire domain that have highest WRF-NARR biases of TMAX and TMIN. All these grid points are found at the upstream (west) direction of mountain peaks over the western U.S., and with > 40% WRF-NARR precipitation bias.

3.4 Köppen-Geiger Classification

The Köppen-Geiger classification is the most frequently used climate classification and it categorizes climate zones based on seasonal mean precipitation and temperature (Kottek et al., 2006). As the climate changes, changes of in precipitation and temperature makes local climatologies vary through time, which makes the Köppen-Geiger zones change. The historical 1951-2000 climate zones are representative of both historical and projected simulations in this research in order to keep extreme zone-by-zone behavior between the historical and projected simulations comparable. The classification is obtained online (`http://koeppen-geiger.vu-wien.ac.at/usa.htm`). Names of zones are made from three letters that represent main climate, precipitation, and temperature, respectively. Table 3.1 lists the names of zones that are chosen in contiguous U.S. and the climatology each zone represents. Fig. 3.2 are colored maps of zones with pixels from the downloaded shapefile, which has a different grid spacing from WRF. In total 12 zones are chosen from 3 main climate types: B class for arid climate; C class for warm climate; and D class for climate with

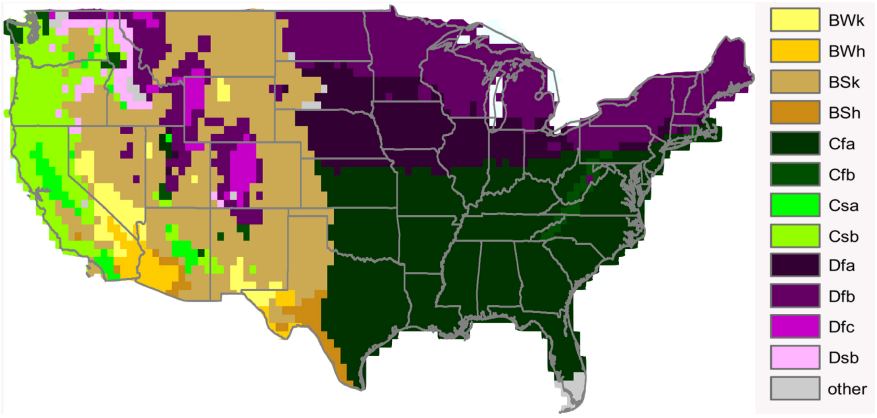

Figure 3.2: Chosen climate zones over contiguous United States based on Köppen-Geiger classification.

snow during winter. Some zones like the tropical climate zones over southern Florida are excluded from the extreme analyses. The lack of data points lead this climate zone insignificant for extreme analysis, especially considering the high precipitation bias. These zones are colored grey on Fig. 3.2.

Table 3.1: Climatology for each Köppen-Geiger climate zone

Name of Zone	Main Climate	Precipitation	Temperature	Number of points (% of domain)
BWk	arid	desert	cold arid	159 (1.92%)
BWh	arid	desert	hot arid	136 (1.64%)
BSk	arid	steppe	cold arid	1695 (20.45%)
BSh	arid	steppe	hot arid	134 (1.62%)
Cfa	warm	fully humid	hot summer	2625 (31.67%)
Cfb	warm	fully humid	warm summer	205 (2.47%)
Csa	warm	summer dry	hot summer	120 (1.45%)
Csb	warm	summer dry	warm summer	504 (6.08%)
Dfa	snow	fully humid	hot summer	911 (10.99%)
Dfb	snow	fully humid	warm summer	1567 (18.90%)
Dfc	snow	fully humid	cool summer	140 (1.69%)
Dsb	snow	summer dry	warm summer	93 (1.12%)

Chapter 4

Results

Bias corrected climatic variables are employed for the different types of extreme analysis. In this section, we examine the difference of extreme thresholds between historical and projected simulations. We also evaluate the frequency and intensity of extremes, and their spatial distribution and temporal trends. PDFs of frequency and intensity of variables within every Köppen-Geiger climate zone help to reveal the dependence of the extreme frequency and intensity to regional climate. Lastly, we explore the historical and the projected durations and frequencies of multi-day heat waves happening within each climate zone.

4.1 Percentile thresholds and their differences

Fig. 4.1 and Fig. 4.2 are the 90%, 95%, and 99% extreme threshold maps for PR, TMAX, and TMIN in the historical and projected simulation, respectively.

In the historical simulation, greatest precipitation thresholds occur over the Gulf States, which have magnitude from 30 mm for 90% threshold to over 80 mm for 99% threshold (Fig. 4.1a, d, ang g). Highest TMAX thresholds are found over the southwestern and central U.S., with value from 312 K for 90% to 315 K for 99% thresholds (Fig. 4.1b, e, and h). TMIN thresholds distributes by latitude. Highest TMIN thresholds are over souther U.S. and they decrease towards north. In 90% extreme map, the TMIN threshold over the northern U.S. is below 254 K and threhold over the

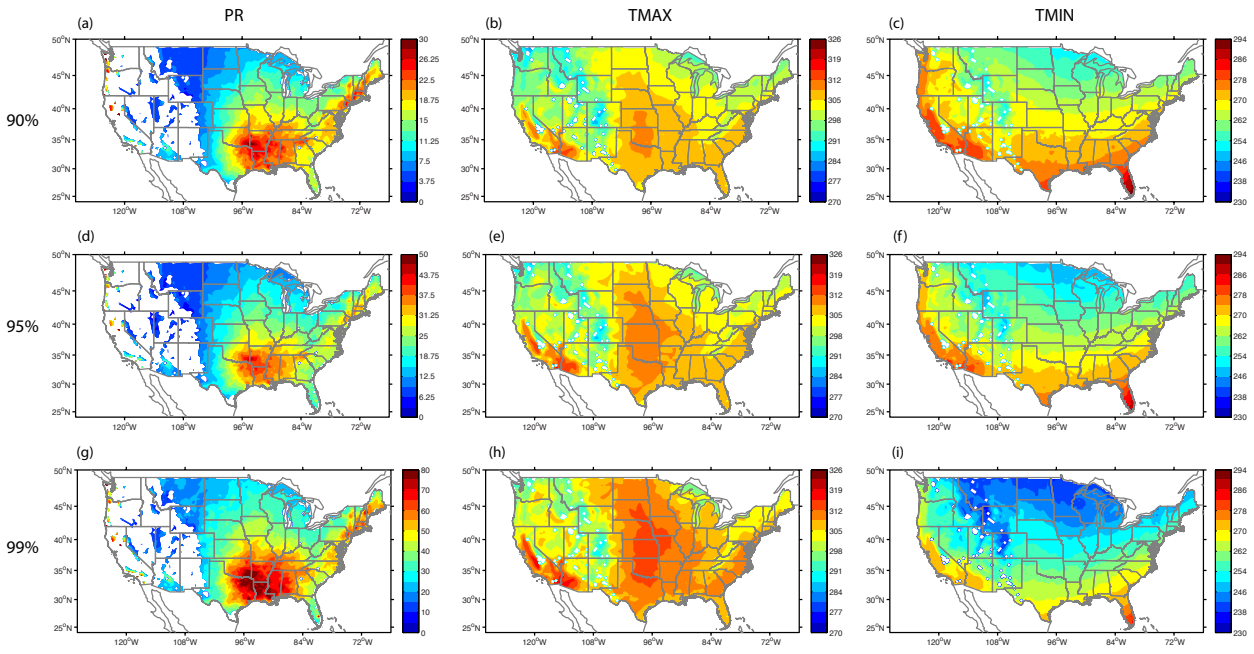

Figure 4.1: Historical extreme values corresponding to the 90th, 95th, and 99th percentile of distribution for PR (left panel), and TMAX (middle panel), and to the 1st, 5th, and 10th percentile of distribution for TMIN (right panel).

southern U.S. is above 280 K. These thresholds drop to under 240 K over the northern U.S. and nuder 270 K over the southern U.S. in the 99% extreme map.

In the projected simulation (Fig. 4.2), the spatial distributions of extreme thresholds patterns are with little differences compared to the distributions that the historical simulation have. But the magnitude of thresholds in the projected simulation are greater for all three climatic variables, including PR, TMAX, and TMIN.

The 90%, 95%, and 99% extreme threshold difference maps of the historical and projected PR, TMAX, and TMIN are shown in Fig. 4.3. The differences are calculated by taking the threshold values (corresponding to the 90th, 95th, and 99th percentile for PR and TMAX, and 1st, 5th, and 10th percentile for TMIN) of the projected simulation minus threshold values of the historical simulation for each grid point. The PR difference is in millimeters (mm), and the TMAX and TMIN difference is in Kelvin (K). For example, a value of 10 mm on the 95% difference map would indicate that the 95th percentile precipitation value is 10 mm greater in the projected simulation than the threshold in the historical simulation.

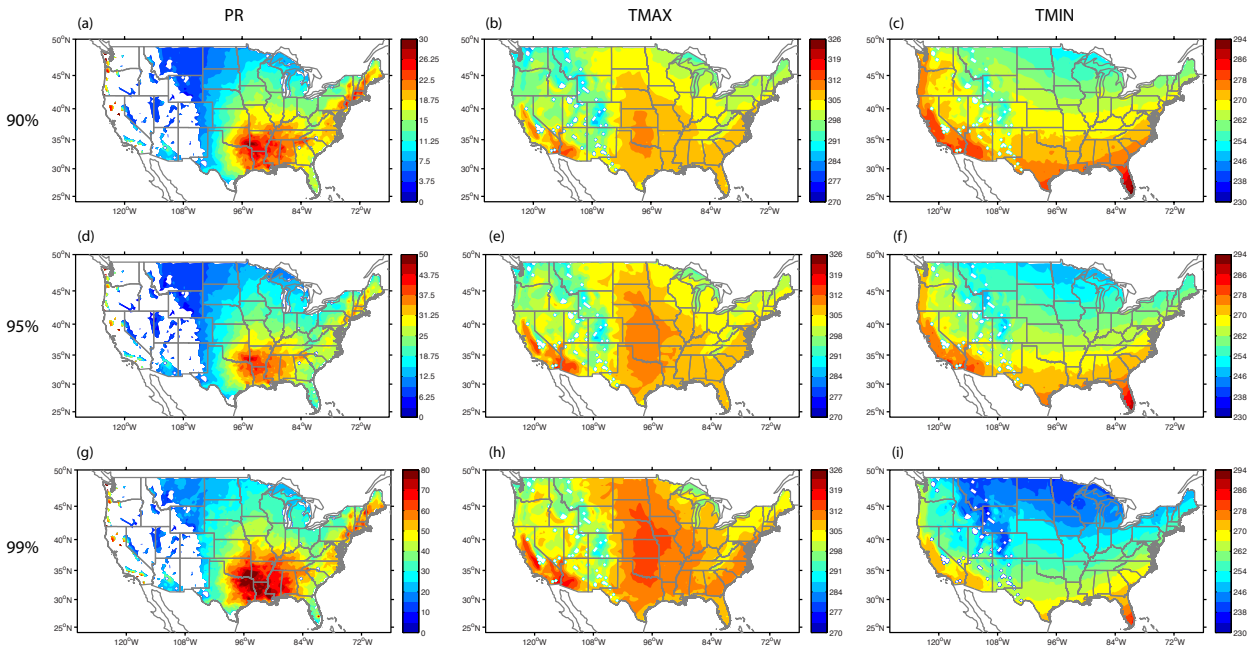

Figure 4.2: As Fig. 4.1, but for the projected simulation.

For precipitation, the threshold differences increase for increasing percentiles (Fig. 4.3a, d, and g). The highest threshold differences are found over the south-central U.S. and southeastern U.S. near the Gulf Coast. Precipitation threshold differences increase from 3 mm in the 90% extreme map (Fig. 4.3a) to over 15 mm in the 99% extreme map (Fig. 4.3g). The increasing differences in precipitation for increasing threshold percentages suggests that the rarer the event, the greater (i.e., more extreme) will be the difference between projected and historical values.

The similar TMAX threshold difference patterns across the different percentiles indicate that differences vary little as percentile increases (Fig. 4.3b, e, and h). Thresholds of the projected simulation are $\sim$3-6 K higher than those of the historical simulation and vary widely over the whole domain. The greatest difference occurs over the north central U.S., just west of the Great Lakes, with a massive area of differences > 5 K on all three maps.

TMIN threshold difference patterns are also largely similar across the different percentiles, although the magnitudes of the differences are greater than the increases in TMAX. This behavior is consistent with a reduction of the diurnal temperature variation in the projected simulation relative to the historical simulation. Greatest differences are found over the west mountainous region and

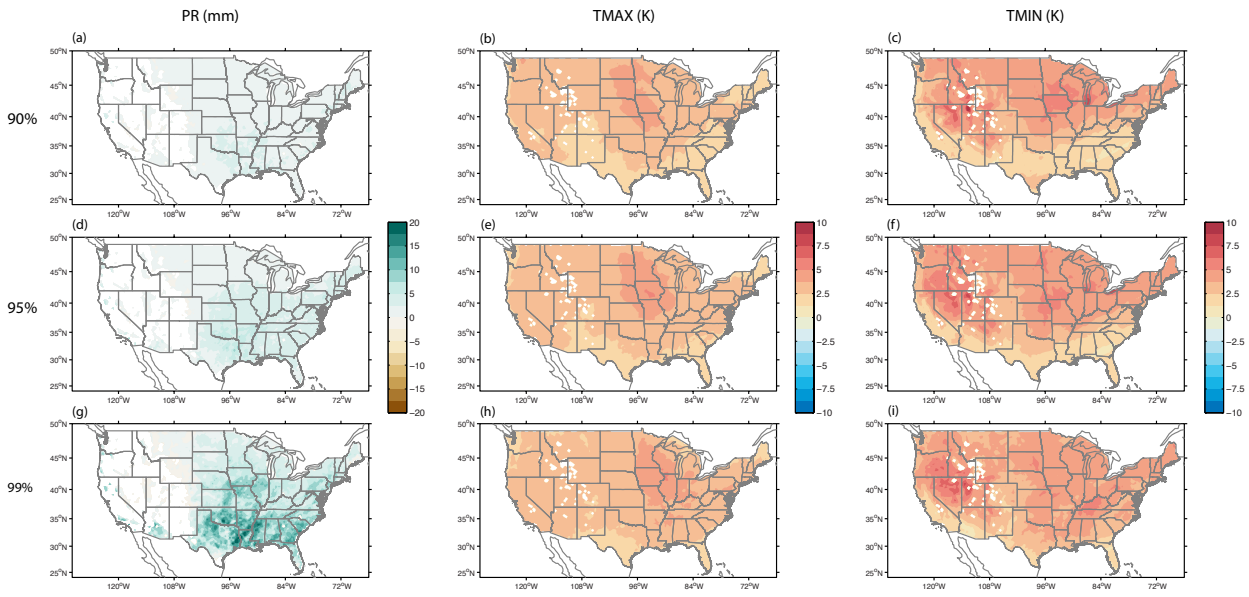

Figure 4.3: Differences between projected and historical extreme values corresponding to the 90th, 95th, and 99th percentile of distribution for PR (left panel), and TMAX (middle panel), and to the 1st, 5th, and 10th percentile of distribution for TMIN (right panel).

northern Great Plain with more than 7.5 K increase of thresholds in the projected simulation for all three percentiles.

In summary, systematic higher extreme percentile thresholds are found in PR, TMAX, and TMIN in the projected simulation, indicating that daily precipitation and daily maximum temperature are more extreme in the projected simulation, whereas daily minimum temperature behavior is less extreme (cold nights become warmer). For the TMAX and TMIN, substantial changes to TMIN thresholds appear more prevalent, a result consistent with lower projected diurnal temperature variation.

4.2 Change of extremes through time

Annual values of frequency and intensity of extreme events are calculated in order to evaluate the change of these quantities with time. The tendencies of extreme PR, TMAX, and TMIN are based on the 90% thresholds evaluated over the entire modeling period for each grid point. Thresholds are calculated the same way as in the previous section. In general, the frequency trend measures if

there are more or fewer extreme events through time, while the intensity trend focuses on whether the extreme events become more or less intense through time. Since extreme frequency and intensity are both calculated annually and are both statistical parameters that depict climate behavior, we have assumed that they are independent sample; in other words, the temporal autocorrelation is neglected. We evaluate the statistical significance of the trends of the annual frequency and intensity values via Mann-Kendall trend test. The null hypothesis states that there is no significant trend of frequency/intensity of extremes through time, with the significance level of α=0.05. Calculated TMIN intensity is multiplied by -1 before mapping so that an increasing trend of extreme TMIN intensity represents a nighttime temperature that is becoming cooler through time. In this way, an increasing intensity trend indicates a trend of more extreme conditions with time in the same manner as the PR and TMAX trends.

We also explore the trend seasonlly, providing a comparison between the seasonal and annual trends, in order to find the attribution of seasonal alteration of extreme behavior to the annual extreme trends.

4.2.1 Trends in the historical simulation

Fig. 4.4 shows the spatial distribution of trends for frequency and intensity of the three variables in the historical simulation. The values of frequency are multiplied by 365, converting the original unit of frequency from events/day to events/year, such that the trend of frequency is then events/year^2. The intensity trend is in mm/year for PR and K/year for TMAX and TMIN. Statistically significant regions of positive trend and negative trend are outlined with red line and black line respectively.

Fig. 4.4a shows that over most of U.S., and trend in PR frequency is negligible (absolute trend value < 0.01 events/year^2). A statistically significant region of negative trends is located over South Dakota and Nebraska, although the trend magnitude is small (> -0.015 events/year^2). On the other hand, the intensity trend is noisy (Fig. 4.4b). Only the New England region exhibits a systematic increase in intensity (> 0.075 mm/year).

Trends in TMAX exhibit more organized patterns than the PR trends. The patterns of frequency and intensity look similar (Fig. 4.4c and Fig. 4.4d). Increasing trends of both frequency and intensity cover much of the contiguous U.S. except for regions over the southwest and northwest U.S., which exhibit negligibly slight decreasing frequency and intensity trends. Significant increasing regions of frequency and intensity cover most of the area to the east of Rocky Mountains, with the highest trends occurring over the northern plains (frequency > 0.019 events/year^2 and intensity > 0.05 K/year). Although the bias in the temperature variables is not as great as the precipitation bias, the large precipitation bias in the mountain regions of the western U.S. casts at least some doubt on the behavior of temperature variables. In particular, we suspect that overestimating the precipitation may lead to underestimates of TMAX.

TMIN frequency and intensity also exhibit organized trends (Fig. 4.4e and Fig. 4.4f). Statistically significant regions of decreasing TMIN frequent occur over most of the country. The most negative trend is found over the mountain west, including large areas of Idaho, Nevada, Utah and Arizona that exhibit trends below -0.015 events/year^2. Statistically significant TMIN intensity trends are negative over the northern and southeastern U.S. The statistically significant decreasing trends over the north-central U.S. and southeastern U.S. have trend magnitudes below -0.05 K/year. Over large areas, both TMIN frequency and intensity are found decreasing over time, indicating that TMIN extremes have become both less frequent and warmer through time.

For seasonal trends, Fig. 4.5 exhibit the trend of precipitation seasonally. Most maps of both the frequency and intensity trends show no systematic patterns. The frequency trends are slight in four seasons, and intensity trends exhibit bands with great postive and negative trends expanding from northeast to southwest. Summer frequency map (Fig. 4.5c) are found a large statistically significant region with negative trend over north central U.S., which coincides with the statistically significant region in annual trend map. Winter intensity map (Fig. 4.5h), on the other hand, shows the statistically significant positive trend over New England as the annual trend does.

Fig. 4.6 are the seasonal trend maps for TMAX. Both the frequency and intensity maps show strong positive trends over large statisticaly significant regions. Winter and spring have smaller

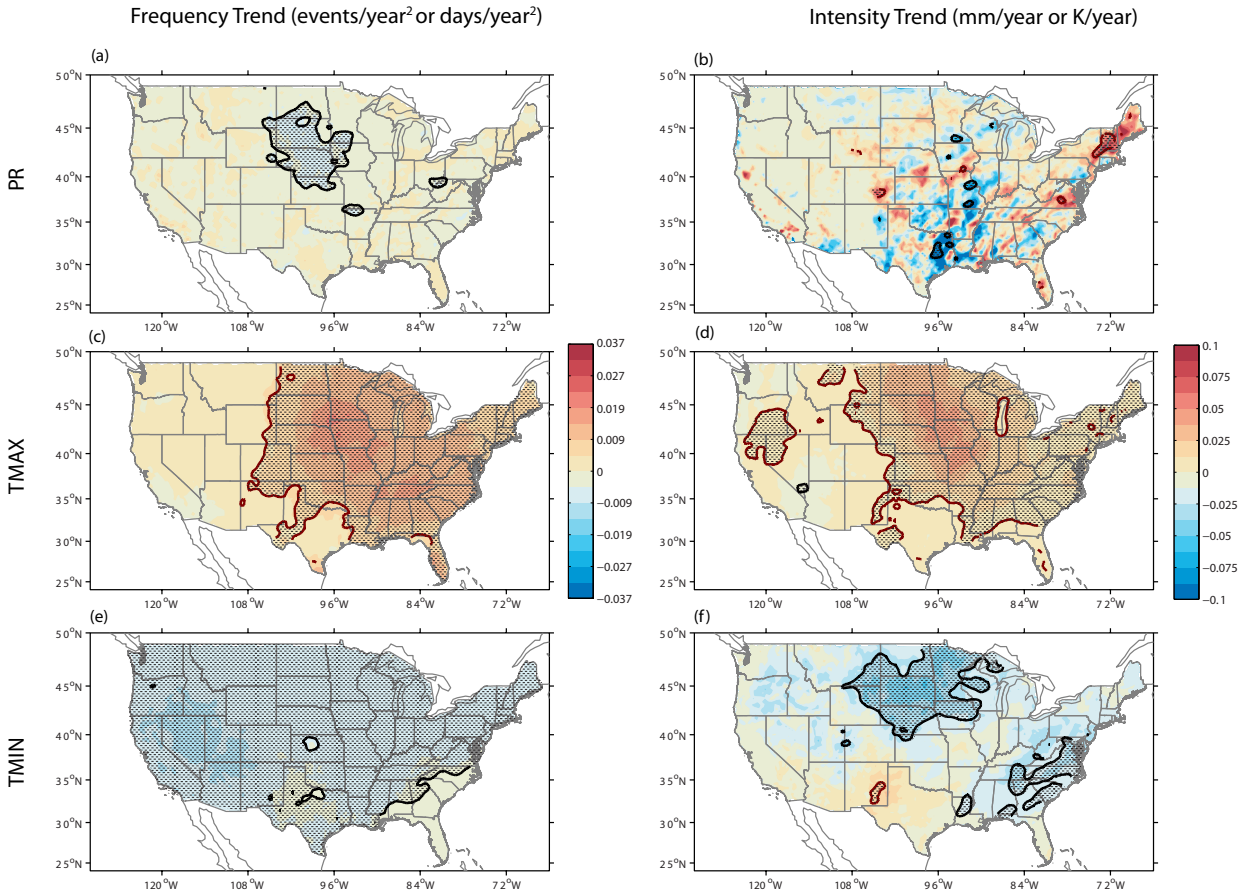

Figure 4.4: Contour maps of the frequency trend of PR, TMAX, and TMIN extremes (left panel), as well as the corresponding intensity trend (right panel) in the historical simulation. Dotted regions outlined by red contour lines are tested significant for positive trend, and regions outlined by black contour lines test significant for negative trend.

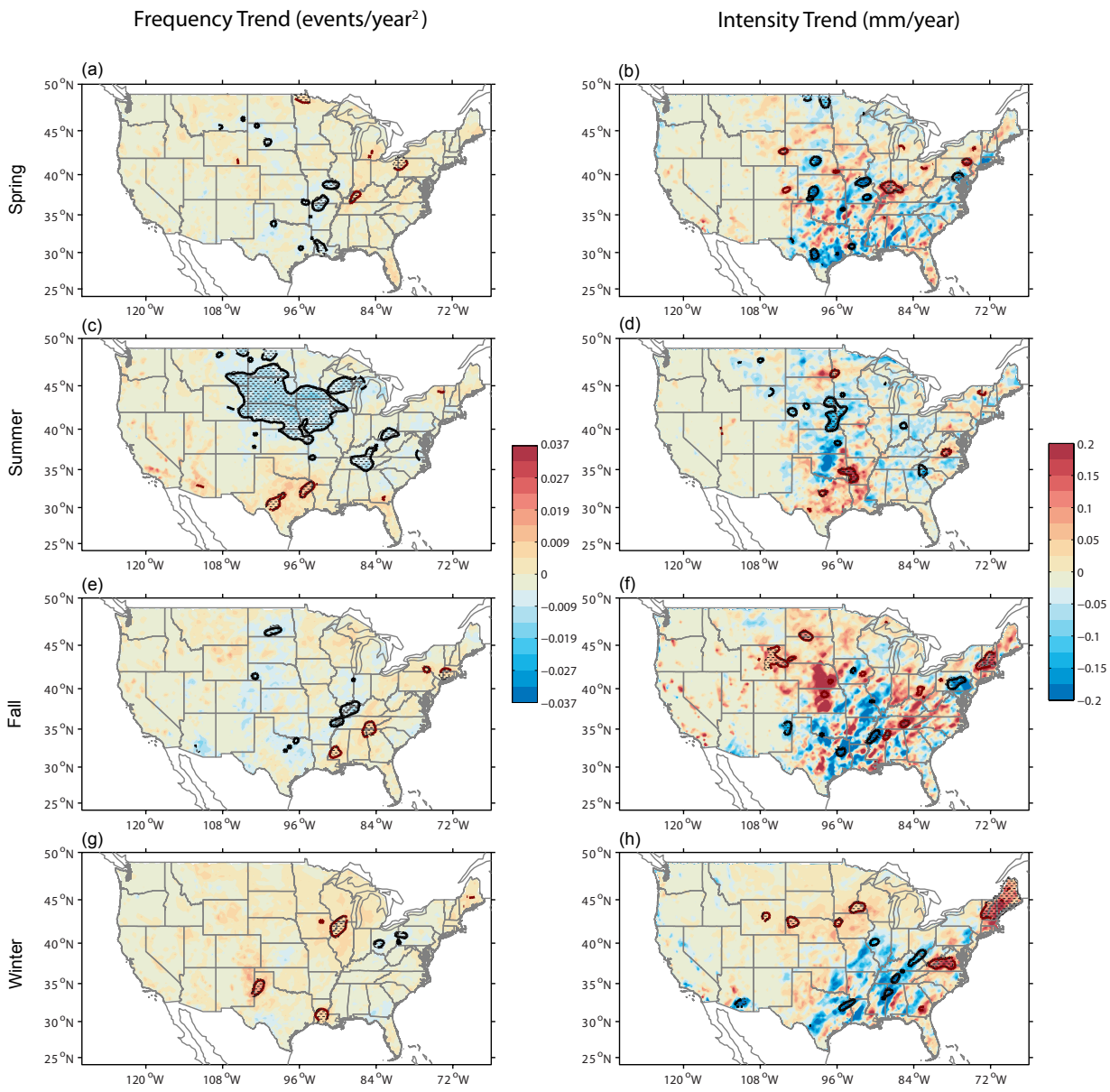

Figure 4.5: Contour maps of the frequency trend of PR in four seasons, as well as the corresponding intensity trend (right panel) in the historical simulation. Dotted regions outlined by red contour lines are tested significant for positive trend, and regions outlined by black contour lines test significant for negative trend.

statistically significant regions than do summer and fall, for both the frequency and intensity. As for annual trends, most statistically significant positive seasonal trends are located over the area to the east of Rocky Mountains.

Generally, the contiguous U.S. exhibits negative trends of TMIN frequency and intensity, but the statistically significant area of is less in spring and summer than those in fall and winter. Moreover, the TMIN positive intensity trend in spring is positive over the north-central and the southern U.S. (Fig. 4.7b), and in summer over the southeastern U.S (Fig. 4.7d). Fall exhibits the greatest negative trends of TMIN, which covers the most of the study area.

A similar analysis based on observational data performed by Wilson et al. (2014) found that the change of extreme precipitation events through time not only exhibits a negative trend, but also seasonal variations. A positive trend in extreme TMAX events and a negative trend in extreme TMIN events are also found. In our results, as the trends for extreme TMAX and TMIN are found similar to that by Wilson et al. (2014), the only season with an increasing trend is spring in this research, while the other three seasons show unchanged or decreasing trends.

4.2.2 Trends in the projected simulation

Fig. 4.8 illustrates trends for the projected simulation. Slight but insignificant increasing trends of PR frequency (Fig. 4.8a) are widely distributed over the contiguous U.S., with trends less than 0.005 events/year^2. The trend of PR intensity (Fig. 4.8b) is much noisier, with small areas of positive and negative trends located close to each other, Many of these areas have large increasing/decreasing trend magnitudes (absolute values > 0.05 mm/year) and are statistically significant. Although the field is noisy, a couple of southwest-to-northeast oriented swaths of precipitation intensity trends are evident, for example the region of positive trends running from Colorado to Minnesota, and the band of negative trends from southwest Texas to Illinois. We speculate this behavior may arise from trends in the large-scale circulation pattern, although detailed examination of that is beyond the scope of this study.

As in the historical simulation, here too the temperature statistics exhibit more organized pat-

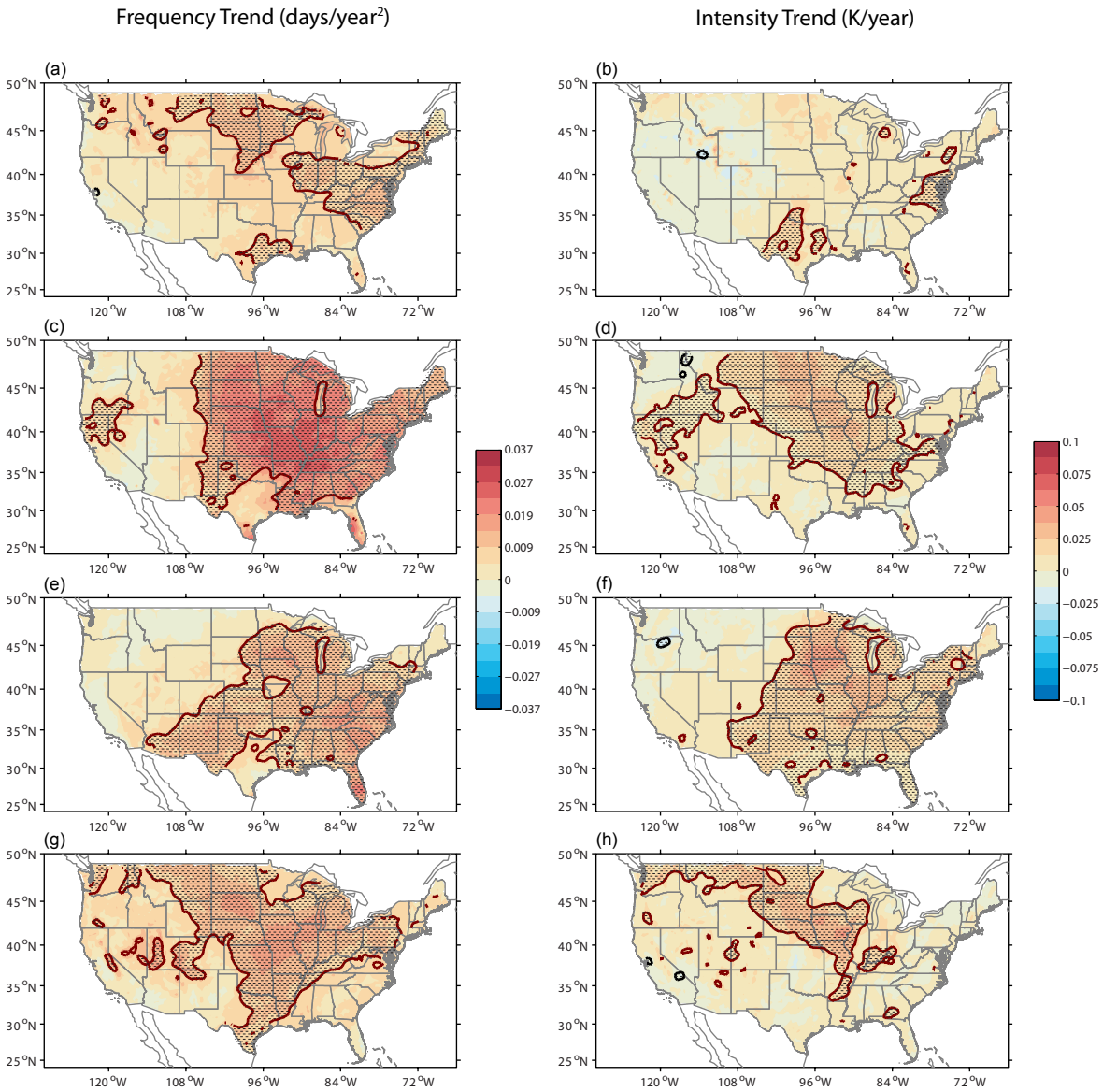

Figure 4.6: As in Fig. 4.5, but for TMAX.

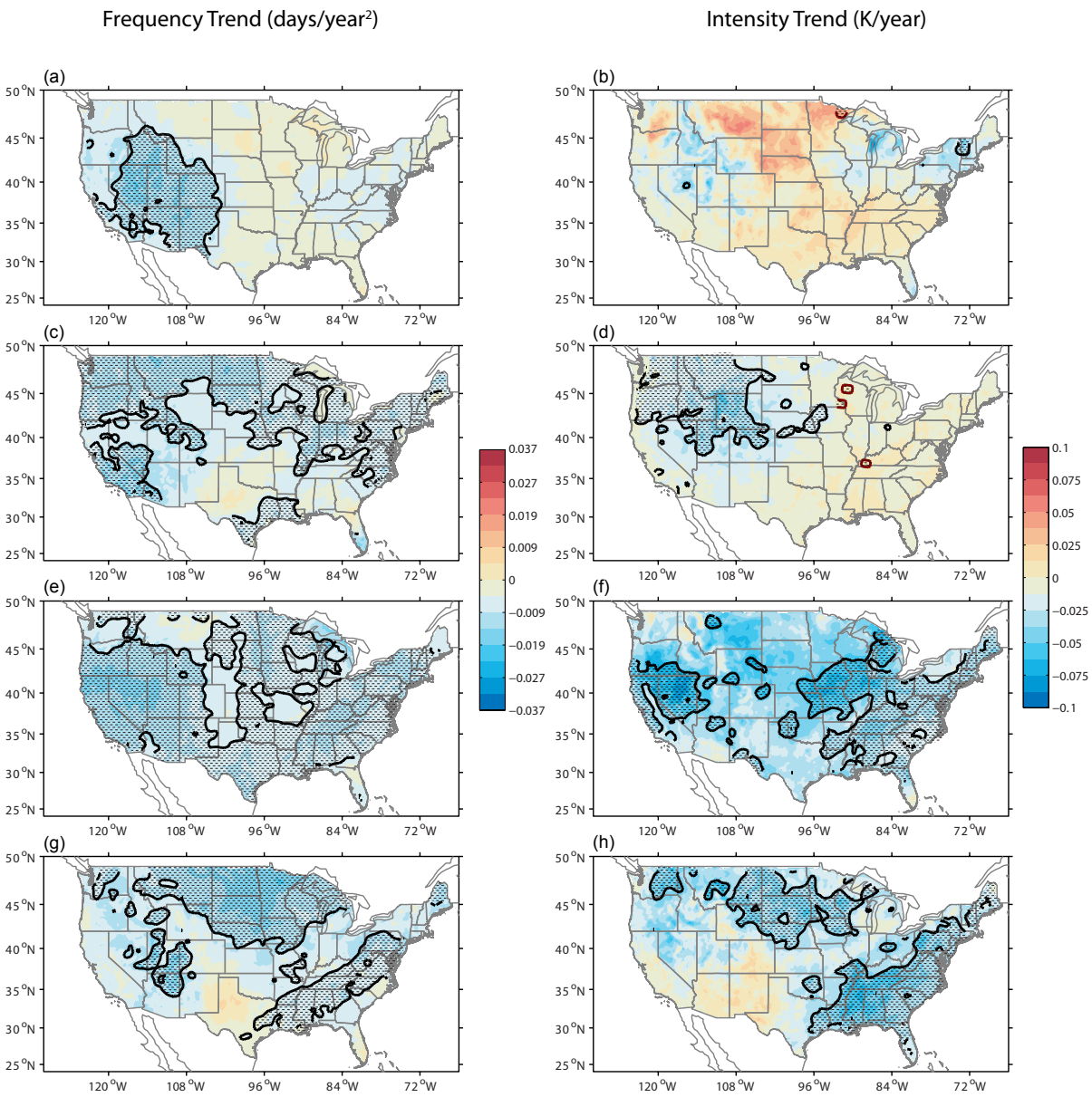

Figure 4.7: As in Fig. 4.5, but for TMIN.

terns than do the precipitation statistics. Uniformly increasing trends are found in TMAX on both frequency and intensity (Fig. 4.8c and Fig. 4.8d). Positive trends increase toward the south, and the greatest positive trend of frequency > 0.02 events/year^2 is found over the southern region of the Gulf States. The TMAX intensity trends vary little over the U.S., with the trend between 0 to 0.02 K/year. The statistically significant area covers much of the domain, except for the northern Great Plains, the Missouri and Mississippi River basins, the Ohio Valley, and the western coastal region. (Fig. 4.8d).

TMIN trends are weak and less uniformly distributed (Fig. 4.8e and Fig. 4.8f). Weak (though largely not significant) positive trends of frequency and intensity (more cold nights and colder nights) are found mainly over north-central U.S. Regions with decreasing trends (fewer cold nights and warmer nights) are along the south boundary of contiguous U.S. for frequency, and north central and north eastern U.S. for intensity. Only regions of negative trends are significant, specifically regions along south border and Atlantic coast (frequency) and small regions over north-central U.S. (intensity).

Seasonal trends of frequency show generally positive trends, but with limited statistically significant area, which coincides with the annual trend map of the frequency (Fig. 4.9). Intensity trend maps display noiser patterns compared to the maps of the historical simulation. Both the freqeuncy and intensity trend maps do not show obvious seasonal variations.

TMAX shows mostly positive trends in the frequency and intensity (Fig. 4.10). Generally, the southern U.S. has greater frequency, and the central U.S. has greater intensity. The winter maps have smaller statistically significant regions than other three seasons on both the frequency and intensity, and it exhibits a slight negative trend of frequency over north central U.S.

TMIN maps (Fig. 4.11) show seasonal variations in the projected simulation. For frequency, summer and fall maps have larger statistically significant area than those in spring and winter, and slight positive trends are found over north central U.S. in spring and eastern and central U.S. in winter. For intensity, regions with positive and negative trends are basically with the same area, but most of statistically significant regions are negative trends.

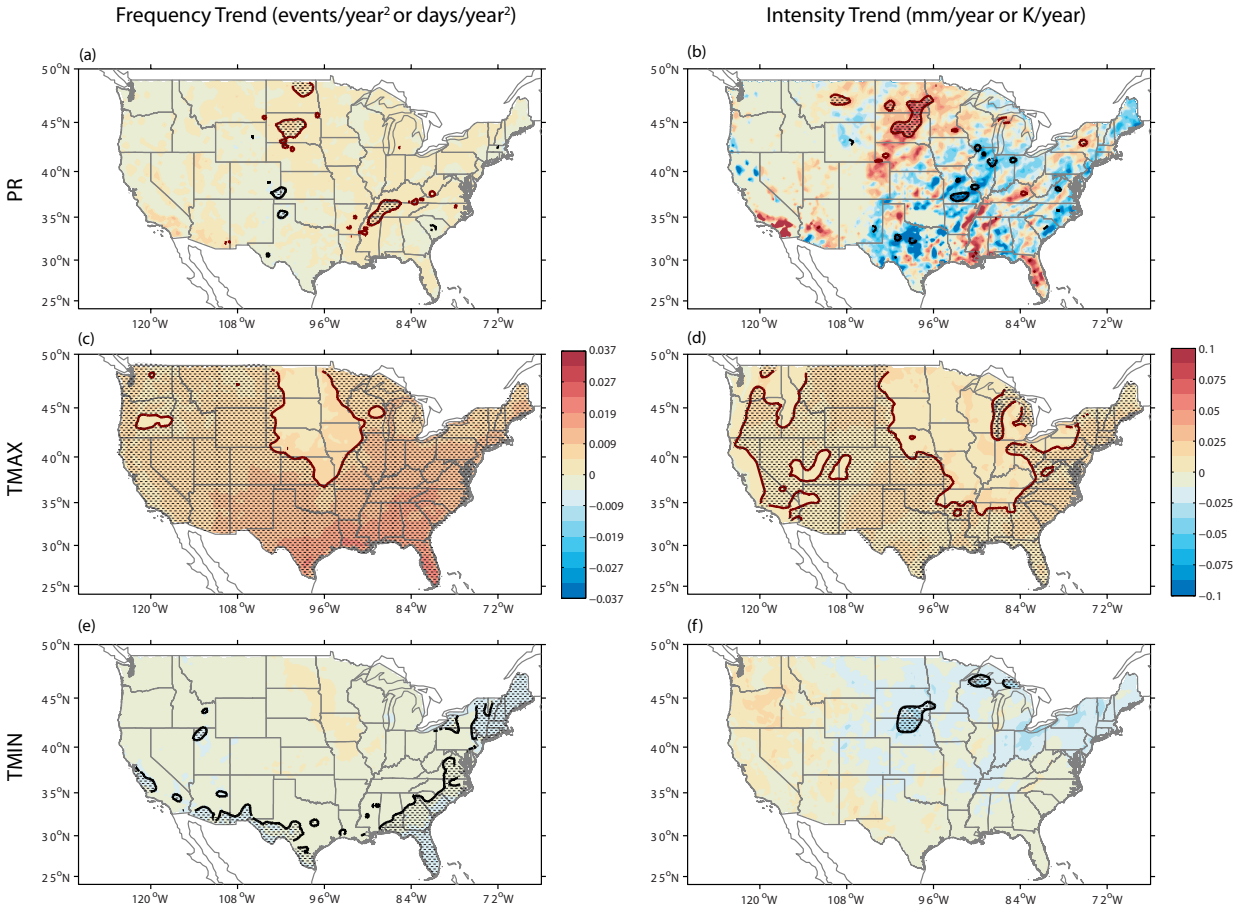

Figure 4.8: As in Fig. 4.4 but for the projected simulation.

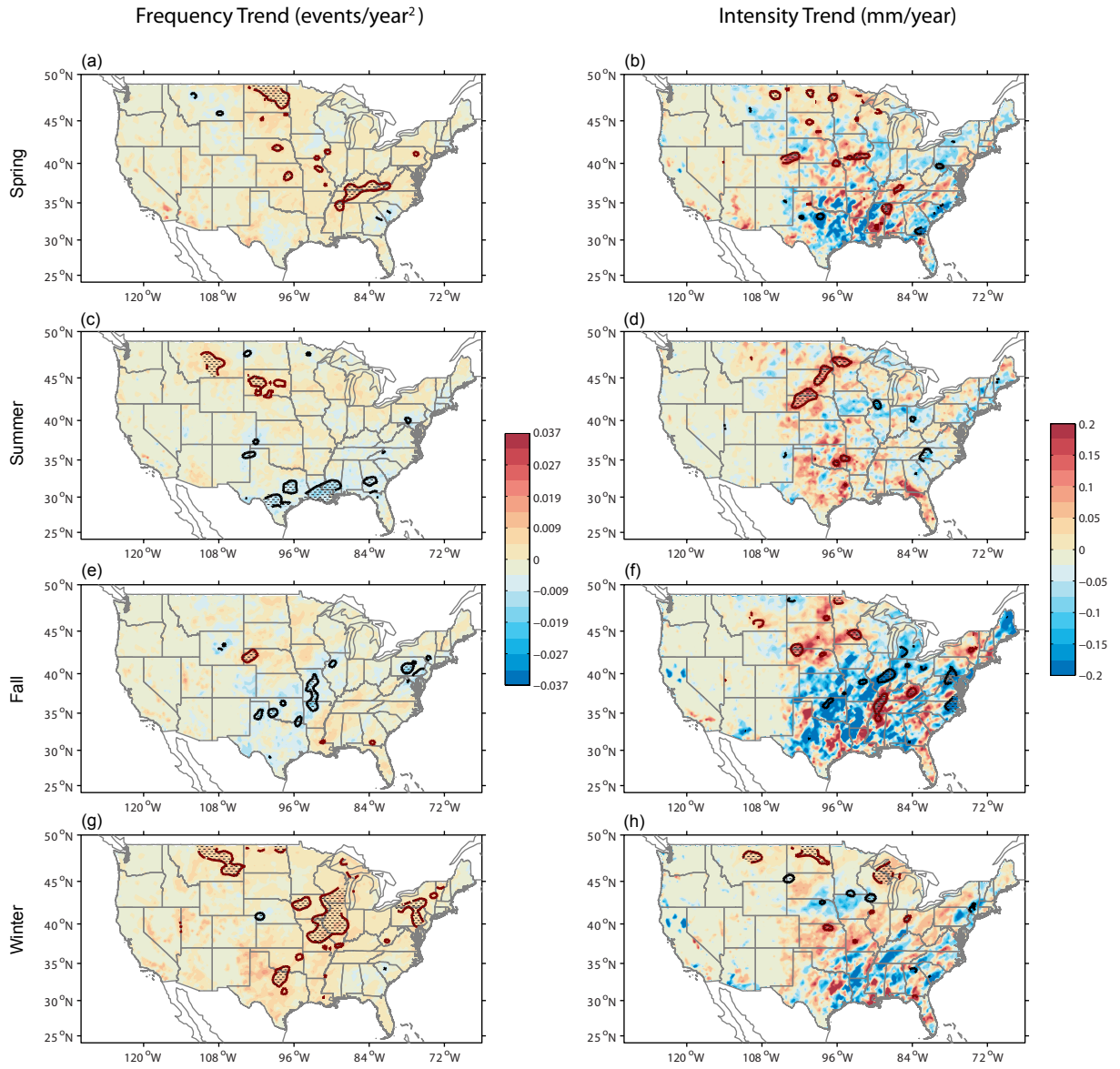

Figure 4.9: Contour maps of the frequency trend of PR in four seasons, as well as the corresponding intensity trend (right panel) in the projected simulation. Dotted regions outlined by red contour lines are tested significant for positive trend, and regions outlined by black contour lines test significant for negative trend.

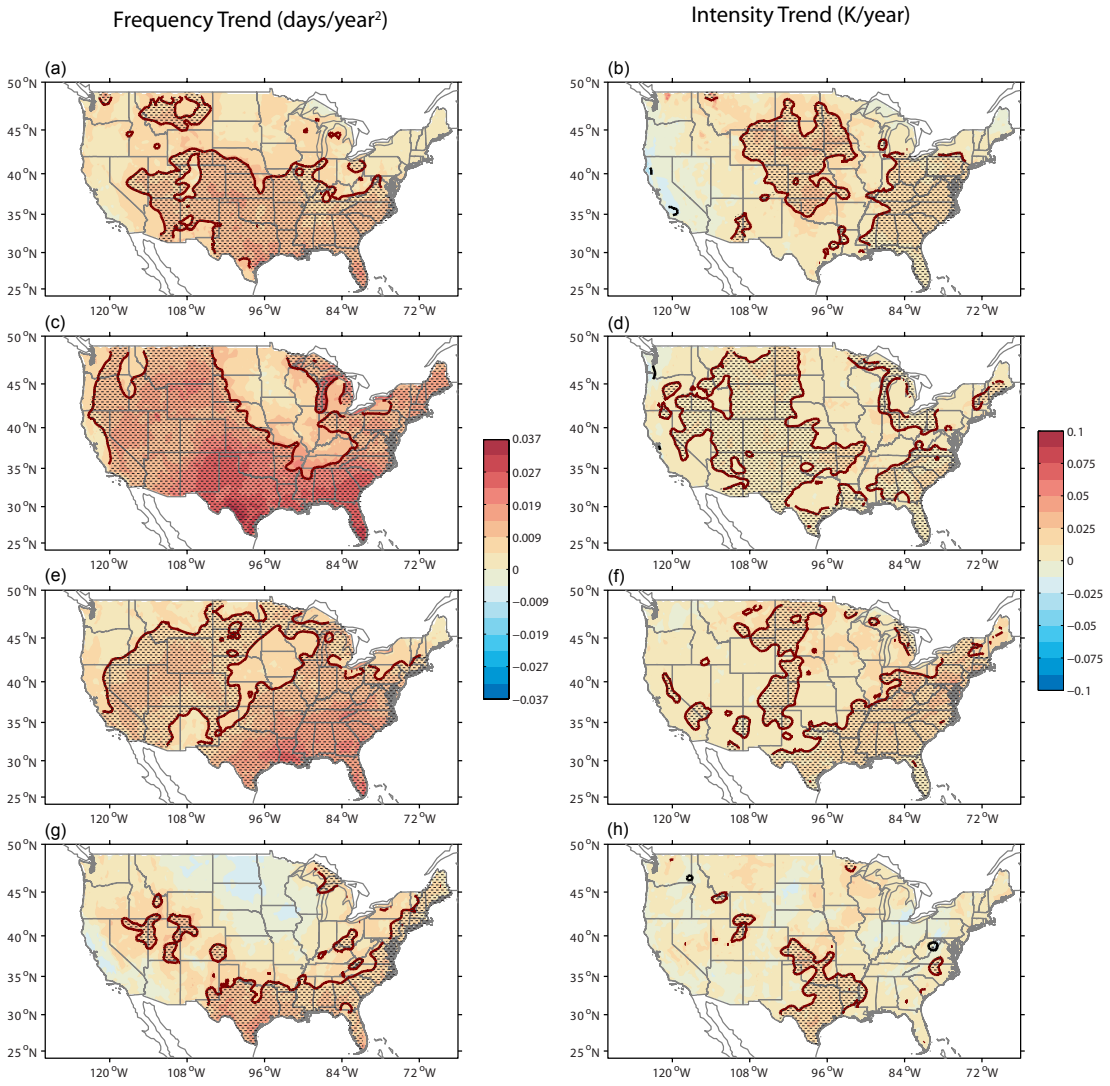

Figure 4.10: As in Fig. 4.9, but for TMAX.

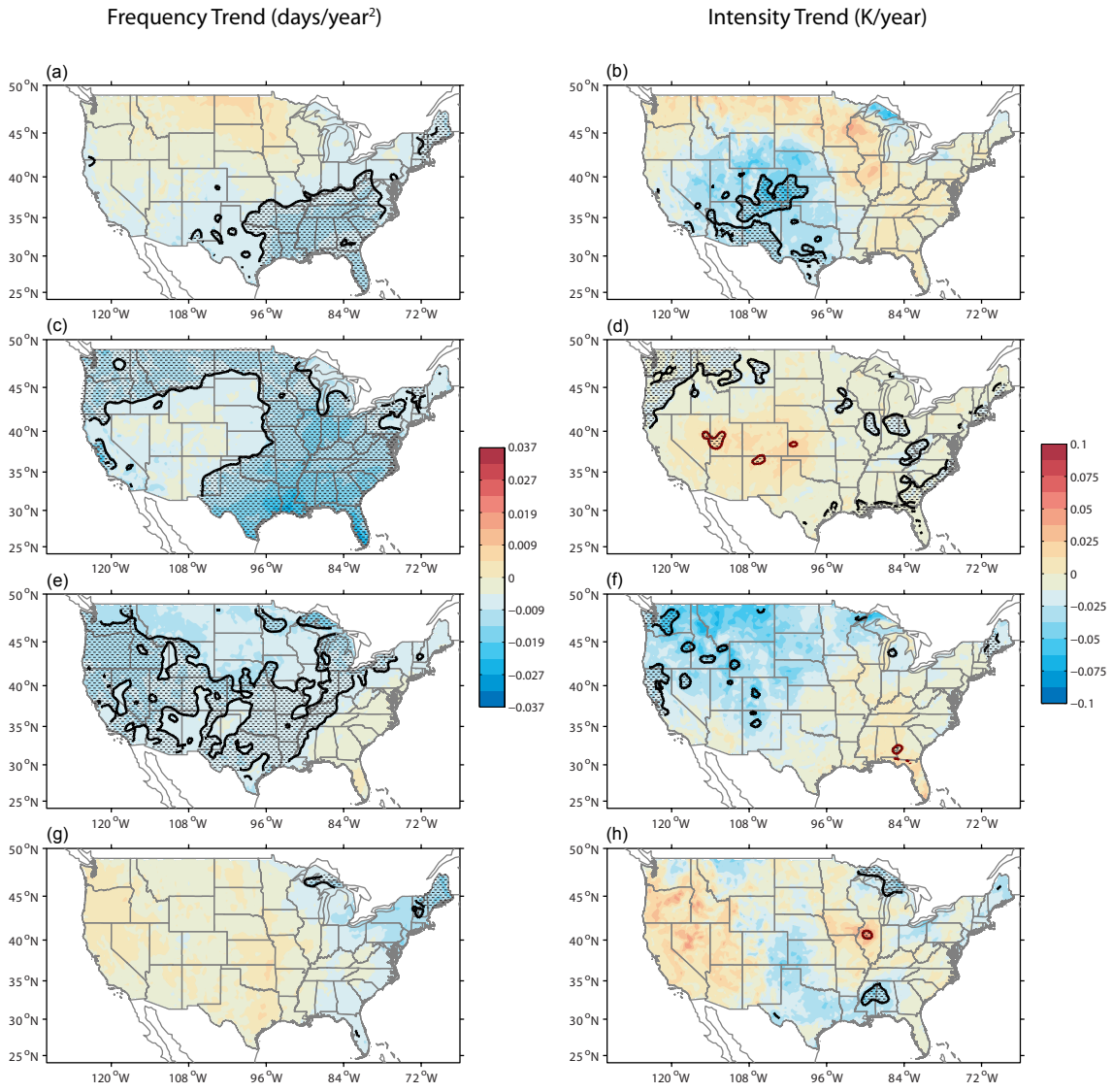

Figure 4.11: As in Fig. 4.9, but for TMIN.

4.2.3 Comparison of the historical and projected trends

Trends of frequency and intensity from three climatic variables are mapped and analyzed. The statistics from the historical and projected simulations differ substantially. Except for a broad region of modest PR frequency trends over Nebraska and South Dakota, the PR frequency trends are weak in both the historical and projected simulations. PR intensity trends, on the other hand, are noisy in both the historical and projected simulations, having small positive and negative trends of intensity located close to each other. Although the field is noisy, some evidence of banded structures is apparent, particularly in the projected simulation, suggesting trends in the large-scale circulation. Seeing in a seasonal perspective, the greatest magnitudes of trends happen during fall in both the historical and projected simulations.

For TMAX, greatest positive trends and widest statistically signifcant regions are found in summer for both the historical and projected simulations. The biggest difference between the historical and projected simulations occurs over the north-central U.S. In the historical simulation, the greatest positive trends occur over the central U.S. In the projected simulation, the positive trends is kept as in the historical simulation, but the greatest magnitudes are found over the southern part, rather than north central U.S. in the historical simulation.

TMIN's negative trends of frequency and intensity are found with higher magnitude and more statistical significant regions during summer and fall. In the historical simulation, TMIN exhibits widely distributed positive trend in frequency and negative trend in intensity, corresponding to fewer, less intense extremes. The broad TMIN frequency and intensity trends in the historical simulation are not present in the projected simulation.

4.3 Extremes in Köppen-Geiger climate zones

In order to gain additional insight into the behavior of the extreme value statistics previously calculated, we aggregate the statistics across climate zones. We employ the Köppen-Geiger climate classification to divide the entire domain into 12 climate zones, which are listed in Table 3.1. As

grid points with > 40% precipitation biases are omitted, there are four zones remaining less than 20% of original number of grid points, which are BWk, Csb, Dfc, and Dsb. We assume these four zones do not contain enough points to meaningfully determine extreme climate statistics, so that we omit these four zones when analyzing precipitation extremes.

In this section, frequency and intensity of extremes are calculated in a slightly different way. 90% extreme thresholds for both historical and projected simulations are calculated by seasonal precipitation and temperature fields from only historical simulation (1950-1999). For PR, we aggregate statistics by seasons (March to May (MAM) for spring, June to August (JJA) for summer, September to November (SON) for fall, and December to February (DJF) for winter). Since most TMAX extremes and TMIN extremes happen during summer and winter, respectively, only TMAX in JJA and TMIN in DJF are considered for temperature extremes.

The box plots show both the historical (red) and projected (blue) simulation distributions. Colored dots over the median lines of some boxes indicate the statistical significance of differences between samples from the historical and projected simulations. We employ the two-sample student's t-test to evaluate statistical significance. Although the samples do not strictly fit to normal distribution, the sample sizes are sufficiently large (> 30) that the t-test is justified. The null hypothesis is that there is no difference between samples of the historical simulation and projected simulation ($\alpha = 0.05$).

Fig. 4.12 shows the springtime frequency and intensity of extreme precipitation distributions. The B class zones, which represent arid climatologies, have the lowest frequency and intensity medians. C class zones, which represent warm and humid climatologies, have higher frequency medians than B class zones but lower frequency medians than D class zones, and also the highest intensity medians (30-40 mm/event). D class zones that represent cold and snowy winter climatologies have frequency medians > 0.05 events/day and intensity medians slightly below 30 mm/event. Within the C class zones, Csa frequency and intensity behave differently compared to Cfa and Cfb. The different behavior of the Csa is largely a function of its coastal location but also may partly be a nonphysical result of the high precipitation bias over the mountainous west.

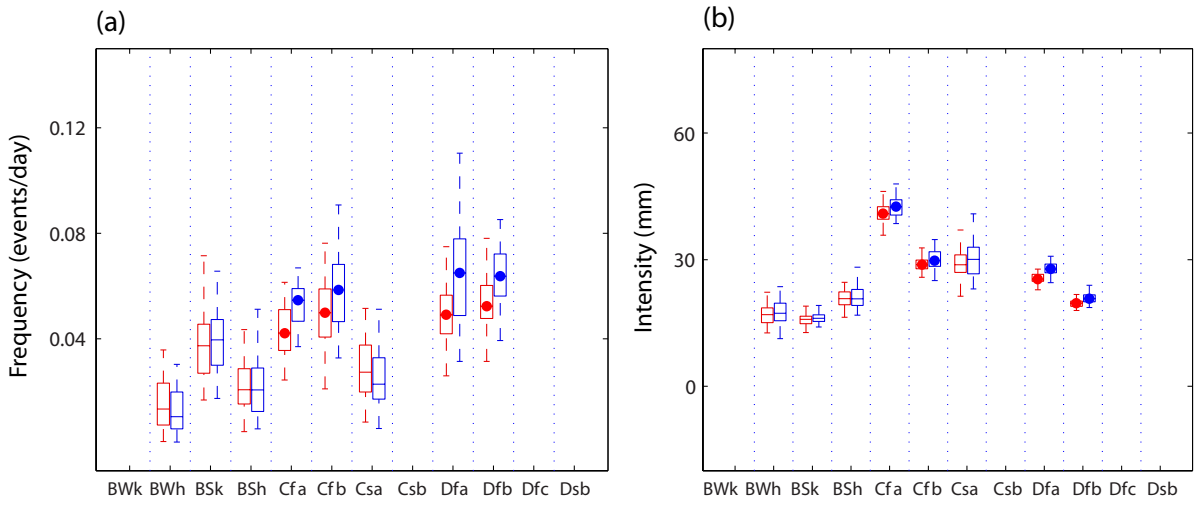

Figure 4.12: Box plots for frequency (a) and intensity (b) of extreme precipitation in spring. Within each climate zone, the red box denotes the historical simulation and the blue box denotes the projected simulation. Colored dots indicate the difference between the two samples in that climate zone is statistically significant.

In all zones, intensity in the projected simulation is greater than the respective historical value, and for most zones frequency is higher, too (BWk, BWh and Csa being the only zones with lower projected frequency). The four zones of Cfa, Cfb, Dfa, Dfb, which together includes most of U.S. east of the Rocky Mountains, have frequency and intensity differences that are tested significant.

Fig. 4.13 shows the frequency and intensity box plots for the summer season. Summer generally exhibits similar frequency and lower intensity than springtime. For B class zones, Bsk has the frequency median about 0.05 events/day while the other two B class zones have medians lower than 0.04 events/day. All zones in C and D classes except for Csa have medians around 0.05 events/day. Intensity medians are all below 30 mm. The historical and projected simulations exhibit little in the way of difference during the summer season, except for a statistically significant frequency and intensity increases of 0.01 events/day and 1 mm/event, respectively, for the Csa zone (which we suspect is dubious because of the precipitation bias over the coastal mountain ranges), and an increase in intensity of 1 mm/event for the Dfb zone.

The median frequencies of extremes during fall are below 0.04 events/day (Fig. 4.14a) and are generally smaller than during spring and summer. Intensity of extremes during fall is similar to

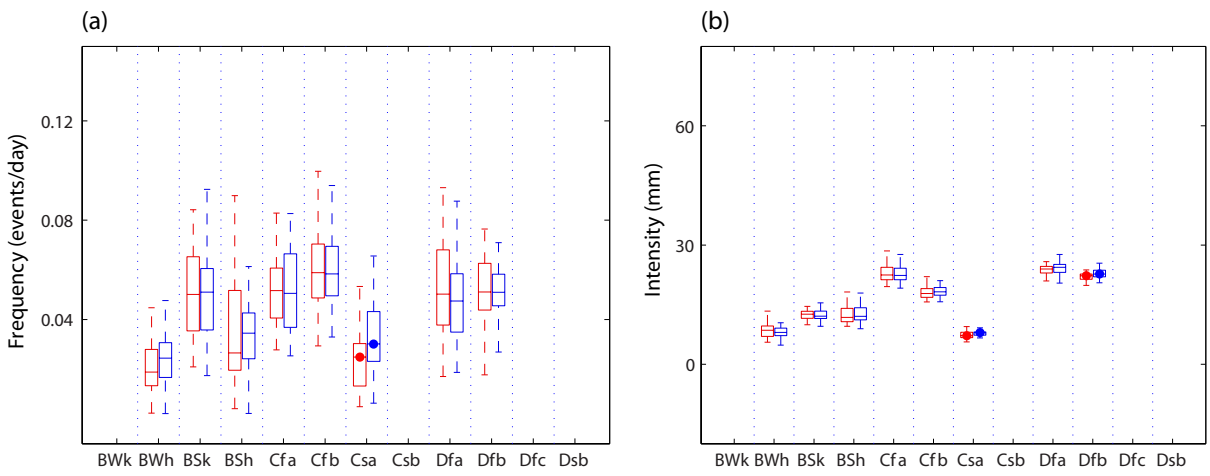

Figure 4.13: Same as Fig. 4.12 except for the season of summer.

spring, with intensity of the C class zones higher than B and D class zones. Significant increases of frequency in the projected simulation is only found only for Bsh, but significant intensity increases are found in 6 zones (Bsk, Bsh, Cfa, Cfb, Dfa, and Dfb), which together cover the most of contiguous U.S.

Fig. 4.15 shows wintertime box plots of frequency and intensity. Winter has relatively lower frequency than spring and summer but higher frequency than fall, especially for C and D class zones, which have frequency medians above 0.04 events/day for all zones in these two classes. Intensity medians are slightly higher than three other seasons in B and D classes, but slightly lower than that fall in C class. Most zones have both significant higher frequency and intensity values in the projected simulation. The only two exceptions are insignificant frequency increase in Bsh and the intensity increase in Dfb.

In summary, precipitation extremes generally have the lowest frequencies in B class zones, relatively higher frequencies in C class zones, and the highest frequencies in D class zones for all four seasons. On the other hand, C class zones have the highest precipitation intensities in all four seasons, while intensity medians in B and D class zones are lower and similar to each other in magnitudes. These consistency of frequency and intensity in all four seasons patterns basically reflect the main climatic features of each climate zone hold. Comparing historical and projected

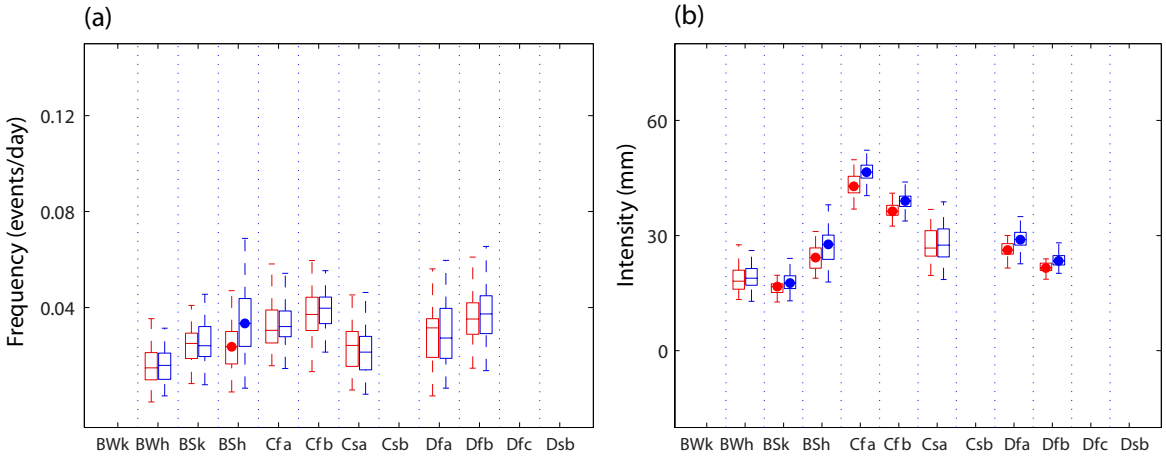

Figure 4.14: Same as Fig. 4.12 except for the season of fall.

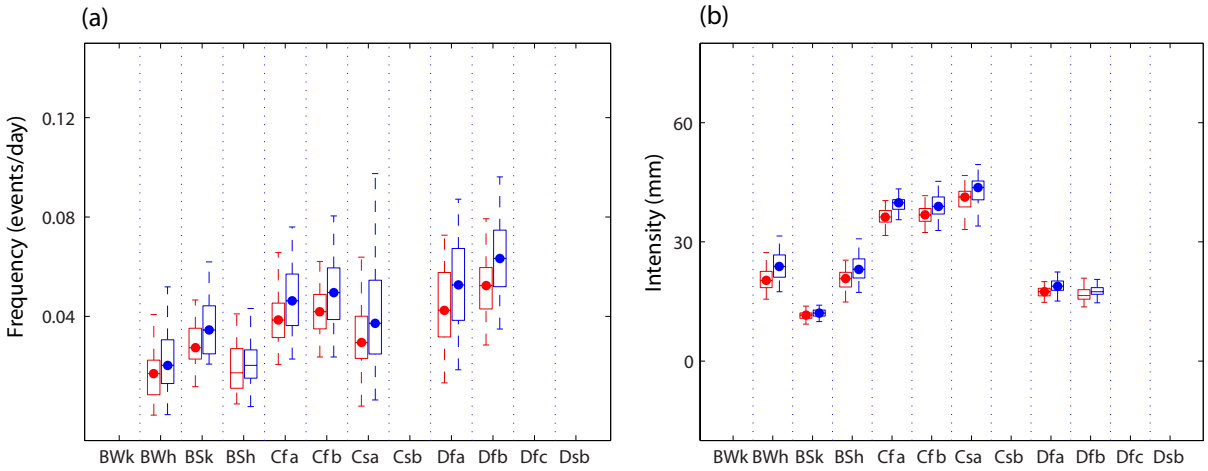

Figure 4.15: Same as Fig. 4.12 except for the season of winter.

simulations, most zones show increases of frequencies and intensities in the projected simulation, although not all differences are statistically significant. There are more statistically significant intensity increases than frequency increases in all the four seasons, but the relative increase in frequency is somewhat greater than the relative increase in intensity. This result suggests that increasing extreme precipitation is manifested as both an increase in frequency and an increase in intensity. Meteorologically, this would be manifested as both heavier local rainfall processes in the projected simulation, as well as changes to the large-scale circulation pattern that influence the frequency. The increase in intensity across most climate zones, however, does not seem to capture the broad spatial positive and negative intensity trend bands visible in Fig. 4.8 (and to a lesser extent, 4.2b).

For temperature extremes, only TMAX in summer and TMIN in winter are considered, since most TMAX and TMIN extreme events occur during summer and winter, respectively. Fig. 4.16 shows summer TMAX frequency and intensity box plots in both simulations. TMAX has similar frequency medians across most of climate zones, with medians around 0.1 for all zones in the historical simulation. Intensity, on the other hand, varies from zone to zone. The B class zones have relatively higher intensity, and highest intensity occurs in BWh with median above 315 K, lowest intensity is in Dfc zone with the median of around 295 K.

Uniformly higher frequency and intensity of TMAX extremes are showed in the projected simulation, and all the differences reject the null hypothesis in student's t-test. Frequencies in all zones of the projected simulation are 0.1-0.2 events/day higher than in the historical simulation, and the magnitudes of higher TMAX intensity in the projected simulation are mostly within 2 K. Differences in frequency between the projected and historical simulations differ substantially by climate zone. This large dependence on climate zone is not present for intensity, a result that may be due to the small ranges of intensity in both the historical and projected simulations.

Fig. 4.17 shows frequency and intensity box plots for TMIN. TMIN differences between projected and historical simulations do not exhibit the same level of variability across climate zones as does TMAX. TMIN frequency boxes also exhibit little variations across each zones as TMAX.

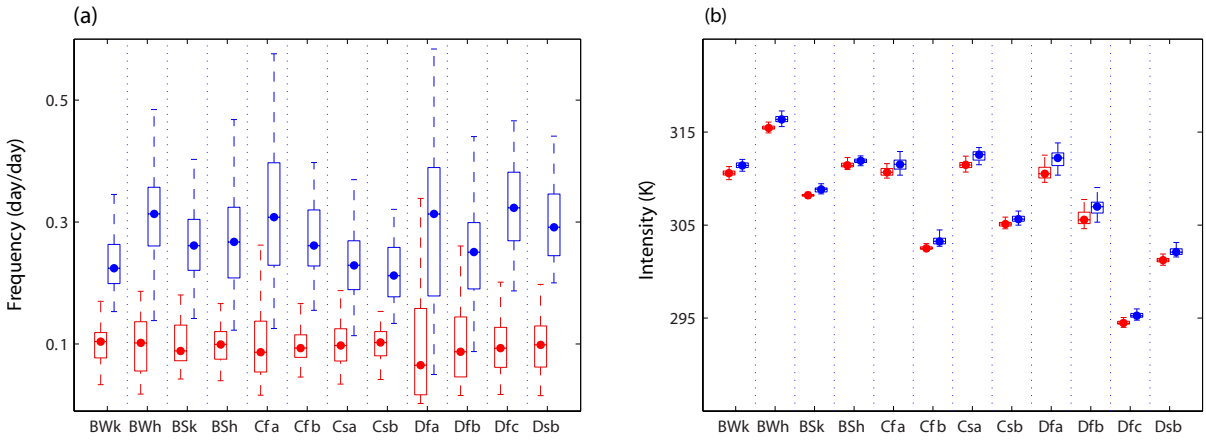

Figure 4.16: Box plots for frequency (a) and intensity (b) of TMAX in summer. Within each climate zone, the red box denotes the historical simulation and the blue box denotes the projected simulation. Colored dots indicate the difference between the two samples in that climate zone is statistically significant.

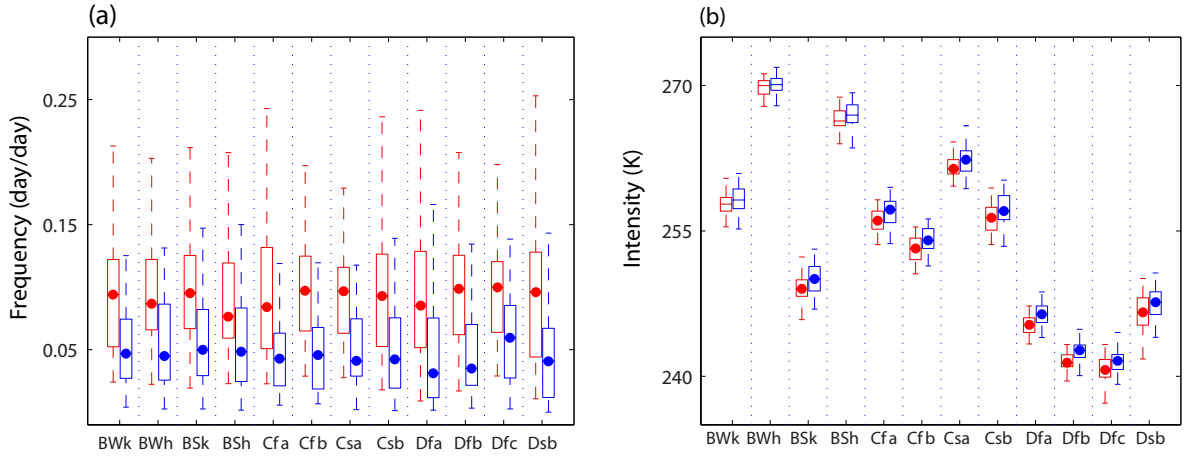

Figure 4.17: Same as Fig. 4.16 except for TMIN in winter.

Historical frequency medians are around 0.09 events/day, and the projected medians around 0.05 events/day. Intensity extremes of TMIN are approximately 2 K higher in projected simulation than the historical simulation, a value roughly consistent across the different climate zones. Frequency and intensity differences between the historical and projected simulations are statistically significant for most of the contiguous U.S. Only BWk, BWh, BSh, which are all small arid zones, have the insignificant projected intensity increases.

Temperature extremes exhibit consistently warmer behavior in the projected simulation. Temperature extremes have higher frequency for TMAX and lower frequency for TMIN, and the intensities of extreme TMAX and TMIN are both higher (warmer) in the projected simulation. For precipitation, the differences in extreme behavior between the projected and historical simulations are reflected in both changes to frequency and to intensity. Differences in TMAX and TMIN, on the other hand, are largely manifested as changes to frequency, in other words a change to the number of events that exceeds the given thresholds. Although the increases in TMAX and TMIN intensity are statistically significant, they are both small (< 2 K/event).

4.4 Quantification of heat waves in terms of Köppen-Geiger climate zones

The previous analysis has been confined to daily events, for example an extreme daily precipitation event or a daily exceedance of maximum temperature. However, it is well known that multiple days of high maximum temperature — heat waves — can substantially impact agriculture and human health (Easterling et al., 2000b; Parmesan et al., 2000). Although there is no universal definition of heat waves, the definition of heat wave we chose in this research was first introduced by Meehl and Tebaldi (2004). Two thresholds of T1 and T2 are defined by the 97.5^{th} percentile and 81^{th} percentile of TMAX values during summer (JJA) respectively in historical simulation. A heat wave event is then distinguished by three criteria: (1) There must have at least three days during the heat wave period with TMAX > T1, (2) averaged TMAX during the period must be greater than T1,

(3) every day during the period must have TMAX > T2. For every grid point, the frequency of heat wave (times/year) and mean duration of heat waves (days) are calculated for both historical and projected simulations. Grid points are categorized into Köppen-Geiger climate zones and box plots are made for each zone. We quantify heat waves in the projected simulation using T1 and T2 established in the historical simulation but recognize that in a warming climate, this will naturally lead to more heat waves of longer duration. This can be simply a result of larger values of TMAX. Expecting that heat waves will be more frequent and have longer durations, we also quantify heat waves based on new thresholds defined adding the increase of mean temperature between the projected and historical simulations to the original T1 and T2 thresholds, which we then term $T1'$ and $T2'$. These two thresholds quantify heat waves independently of the global mean temperature increase, which helps us discern whether the change in heat wave behaviors arises primarily from the increase of mean TMAX, or in creases in the tails of TMAX distributions in the projected simulation.

Fig. 4.18 shows box plots of WRF simulations for the mean duration of heat waves (Fig. 4.18a) and mean number of heat waves per year (Fig. 4.18b) for every Köppen-Geiger climate zone. Medians of heat wave durations in the historical simulation range from 6 to 8 days. C class zones have similar duration medians as B class zones but with larger ranges. Dfa and Dfb have the longest durations of heat waves, with a wide range and maximum values over 20 days. The projected simulation (blue boxes) shows nearly double the heat wave durations of the historical simulation and greater variability within each climate zone.

Box plots of mean number of heat waves per year are mostly from 1.2 to 1.5 times/year in the historical simulation, with modest variation from zone to zone, and the numbers rise to $\sim$3-4 events per year in the projected simulation. Cfa, Dfa, and Dfb zones have the greatest ranges of values, which reflect their large numbers of grid points. For box plots in the projected simulation with $T1'$ and $T2'$, the numbers of heat waves decrease to $\sim$1.2-1.5 events per year, values little different from those in the historical simulation. Cfa, Csa, and Dfa zones in the projected simulation have higher medians than historical simulation, while other zones have lower medians.

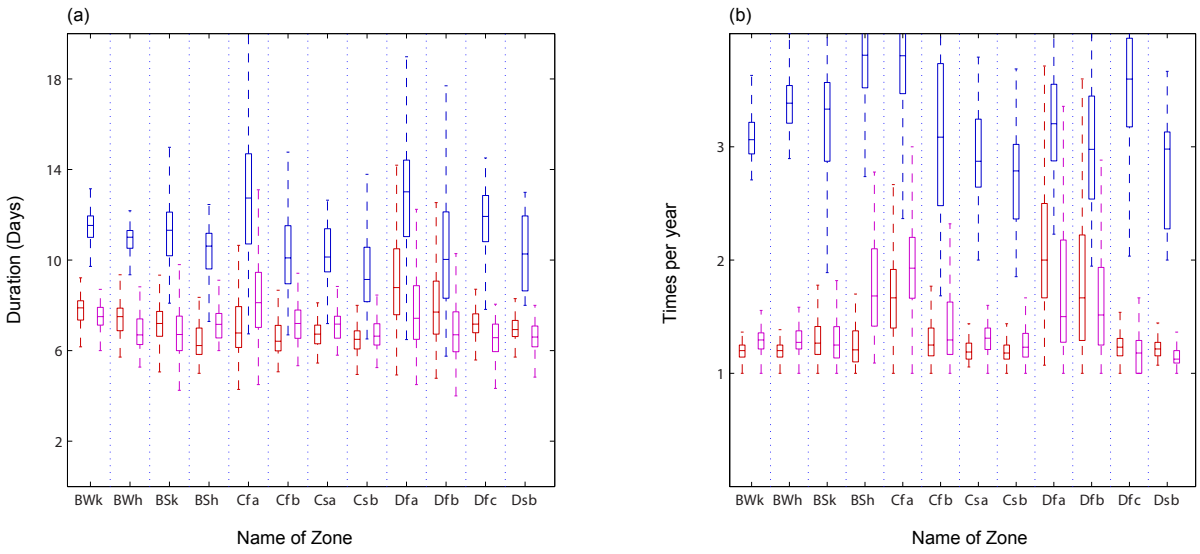

Figure 4.18: Box plots for downscaled mean duration of heat waves (a) and mean number of heat waves per year (b). Red boxes correspond to the historical heat waves, and blue boxes to the projected heat waves calculated from 20^{th} century thresholds, T1 and T2. Purple boxes are for projected heat waves from thresholds T1′ and T2′.

Comparing between these three series of box plots, projected heat waves are more frequent with longer durations. The projected simulation indicates ∼3-4 heat waves that are ∼10-15 days long. The fact that both the projected duration and frequency of heat waves calculated using T1′ and T2′ thresholds vary little from the duration and the frequency of the historical simulation suggests that much of the increased heat wave activity arises simply from an increase in the mean temperature (shift of the entire distribution) rather than the change to the tail of the distribution.

In order to gain more insight into the increase in heat waves in the projected simulation, we extend the analysis to the CESM output used to drive the WRF simulations. Fig. 4.19 shows mean durations (Fig. 4.19a) and mean numbers of heat waves (Fig. 4.19b) per year. In the historical simulation, the CESM medians of mean heat wave durations are 6∼8 days, consistent with the duration simulated by WRF simulation, with little variation across different zones. The projected durations increase to ∼9-14 days with substantially greater variability, values again more or less consistent with the WRF simulation . Using the revised T1′ and T2′ thresholds, the projected medians drop back to ∼8-10 days near the historical durations.

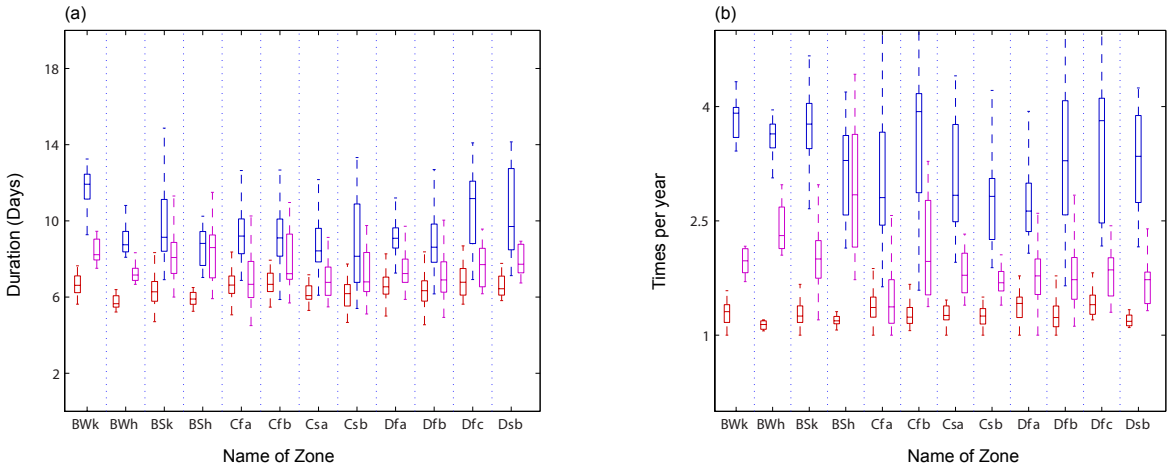

Figure 4.19: Same as Fig. 4.18 except for data from CESM.

The historical simulation averages $\sim$1.2-1.5 heat wave events per year, with little difference across climate zones. As for the increase of durations, the projected mean heat wave numbers increase to $\sim$3-4 events of heat waves per year, with greater variability, especially for the Cfa zone. Calculating mean heat wave numbers using T1$'$ and T2$'$ drops the number of heat waves back to $\sim$2-2.5 events per year, which is approximately $\sim$0.5-1 events higher than the number of historical events per year.

In summary, heat wave behaviors in WRF and CESM are found to be largely consistent in both the historical and projected simulations. This consistency between WRF and CESM suggests that the increase of heat wave severity in the projected simulation of downscaled model output results predominantly from the GCM forcing.

For both WRF and CESM, heat wave durations calculated from T1$'$ and T2$'$ all show magnitudes close to those in the 20^{th} century simulations. Calculated with these thresholds, WRF produces slightly fewer heat waves per year while CESM exhibits slightly more. The greater heat wave indices (both duration and number) in both WRF and CESM projected simulations are largely a result of increases in mean TMAX, rather than a result of increases in the distribution tails.

4.5 Origin of more extreme TMAX events and more severe heat waves

In order to fully understanding the causes of the more extreme TMAX events and more heat waves with longer durations, in this section we plot the PDFs of TMAX for each climate zone in both the historical and projected simulations, and we calculated the difference of mean percentile values based on the historical and the projected simulations. PDFs are presented as violin plots in Fig. 4.20a. The 81^{st} and 97.5^{th} percentile values, as well as mean TMAX, are indicated by lines on the distributions. Difference of these percentile values, as well as the means for each climate zone are presented in Fig. 4.20b and listed in Table 4.1. Fig. 4.20b and Table. 4.1 also include the difference of 90^{th} percentile values, for better explaining the frequency and intensity increase of the extreme TMAX values in the projected simulation.

In B class zones , the increase of the 81^{st} percentile values are the almost same (BWh) or less than the increase of mean TMAX. Mean TMAX increases are around 0.2 K more than the 81^{st} percentile values for BWk, BSk, and Bsh. These three zones also have mean TMAX increases more than the 97.5^{th} percentile values.

In the C class zones, the Cfa and Cfb zones located in the southeast U.S., having different features from Csa and Csb that are located over the west coast. Cfa and Cfb both have mean TMAX increases around 0.2 K greater than 81^{st} percentile value increases. The increase of the 97.5^{th} percentile values, on the other hand, is almost the same as the mean increase in Cfb, but 0.32 K higher than mean increase in Cfa. In zones of Csa and Csb, the 81^{st} and 97.5^{th} percentile increases are both higher than the mean TMAX increases, the magnitude of difference are less than 0.1 K for 81^{st} and 0.4 K for 97.5^{th} percentile.

In the D class zones, the Dfa and Dfb zones show similar increases for both the mean and the 81^{st} percentile. The 97.5^{th} percentile value for the Dfa class, however, increases 0.5 K more than the mean, and both quantities increase similarly for the Dfb zone. Dfc and Dsb show the opposite behavior. Dfc has a higher mean increase than 81^{st} and 97.5^{th} percentile value increases, whereas

for the Dsb zones the mean increases less than do the 81^{st} and 97.5^{th} percentile increases.

Table 4.1: Percentile values and mean difference between projected and historical simulation (projected minus historical)

Name of Zone	81^{st} percentile (K)	90^{th} percentile (K)	97.5^{th} percentile (K)	mean (K)
BWk	2.66	2.60	2.83	2.85
BWh	2.71	2.74	2.79	2.71
BSk	2.83	2.74	2.80	2.94
BSh	2.27	2.22	2.24	2.49
Cfa	2.43	2.60	2.86	2.54
Cfb	2.52	2.48	2.74	2.75
Csa	2.71	2.81	3.03	2.66
Csb	2.86	2.81	2.83	2.77
Dfa	3.49	3.66	3.96	3.46
Dfb	3.02	3.15	3.00	3.01
Dfc	2.77	2.81	2.70	2.85
Dsb	3.53	3.24	3.03	3.21

Fig. 4.20b and Table 4.1 show that the mean TMAX increases in the projected simulation are higher in the D class zones than B and C class zones, indicating that mean temperature increase is larger over the cooler, more northerly regions, than over the south or the desert southwest.

For the two thresholds used to quantify heat waves, the 97.5^{th} percentile value determines how warm each heat wave is, while the 81^{st} percentile value determines how many consecutive days can be included in a heat wave events. Therefore the heat wave frequency and duration are more profoundly affected by the 81^{st} percentile value. Over most of the contiguous U.S. other than northeast, the mean TMAX increase in projected simulation is larger than the increase of the 81^{th} percentile TMAX value. Considering the TMAX PDFs, other than the shifting of the whole distribution toward warmer side (increase of mean TMAX), there are also higher percentage of days in the PDF higher than the mean TMAX in the projected simulation than in the historical simulation.

Greater increases of the 90^{th} and 97.5^{th} percentile values are found over the most of the eastern and western U.S., including big zones like Cfa and Dfa. These greater increases of extreme percentile values indicate more extensive right-hand tail of the TMAX PDFs. This extensive warm (right-hand) tail of the PDF explains the increasing intensity of extreme TMAX values in the pro-

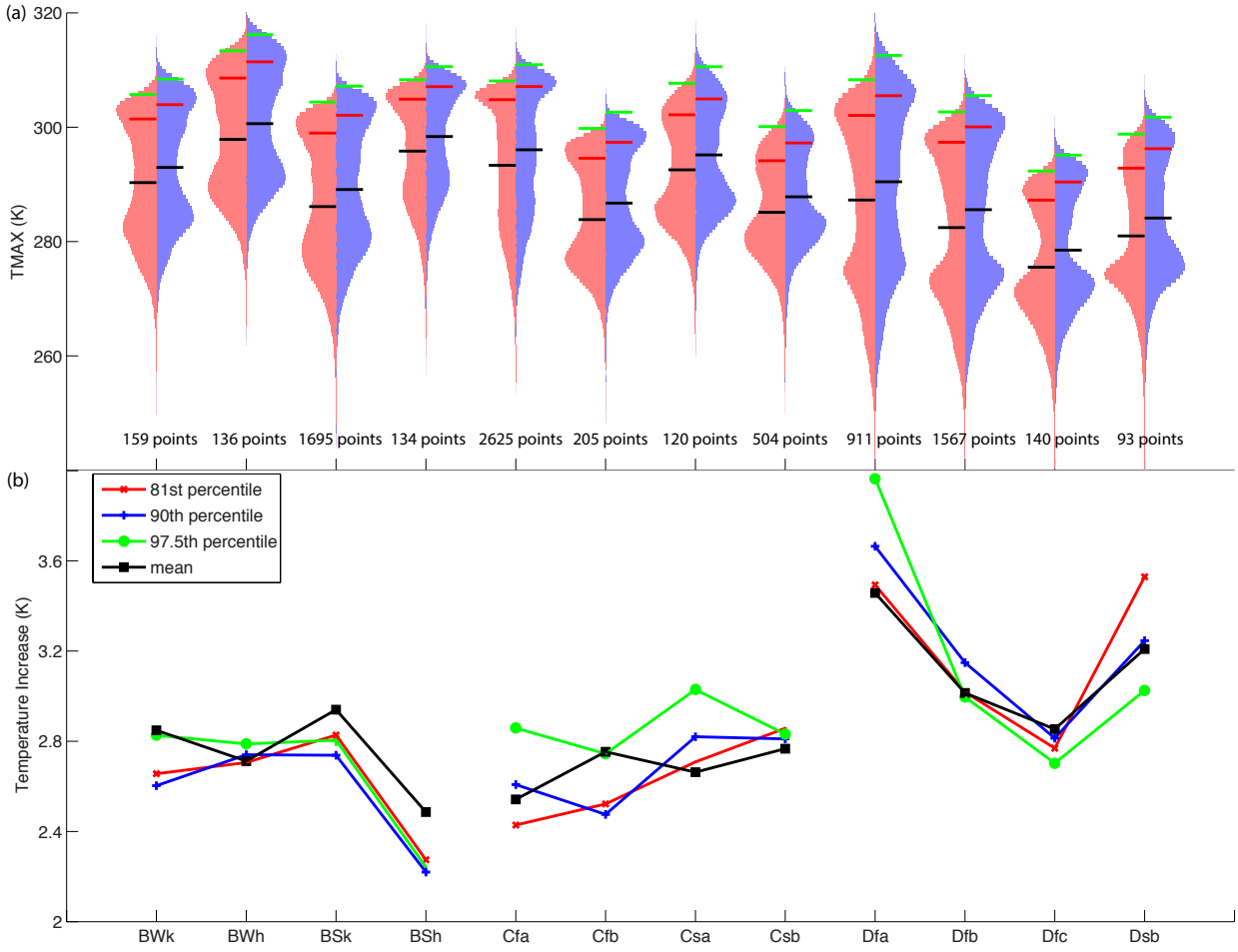

Figure 4.20: (a): Violin plots of TMAX distribution for each climate zone in both the historical (red) and projected (blue) simulation. (b): TMAX increases in the projected simulation compared to the historical simulation of 81^{st} (red), 90^{th} (blue), and 97.5^{th} (green) percentile values, as well as the mean (black) for every climate zones.

jected simulation, which is discussed in section 4.3. This feature contributes to the more extreme temperature behavior in the projected simulation; however its effect on heat wave numbers and durations is very limited compared to the increase in the mean value of TMAX. As a result, the increase of mean TMAX is the predominate cause of more heat waves with longer durations in the projected simulation.

Chapter 5

Discussion

This research employs a dynamical downscaling modeling approach to explore extreme events research over the contiguous Unites States. We force WRF simulations with CESM output for the periods of the second half of 20^{th} and 21^{st} centuries. By defining the frequency and intensity of extreme PR, TMAX, and TMIN based on percentile thresholds (annually or seasonally) for both simulation periods, we are able to quantify the spatial distribution and temporal trend of extremes.

Many aspects of the downscaled simulations behaviors are reasonable. Relative to reanalysis data (NARR), the CESM-WRF dynamical downscaling framework performs better for temperature than precipitation, and better over the eastern U.S. than over the western area. Compared to the original GCM, the downscaling work somehow mitigate the underestimation of precipitation over the Gulf States and the overesitimation of maximum temperature over the central U.S. The precipitation field contains bias, particularly over regions with substantial topography. The precipitation bias may arise for several reasons. First, defects in current RCMs (e.g., the deep convective or microphysics parameterizations) may yield part of the bias. Various model studies have found the overestimation of RCM-modeled precipitation over the western mountainous area (Duffy et al., 2006; Caldwell et al., 2009), and numerical models typically represent better stratiform precipitation then convective precipitation (Maraun et al., 2010). Specifically for simulations in this study, since stratiform precipitation is also biased over mountainous regions, we conducted a number of

sensitivity simulations in order to reduce the substantial precipitation bias over high topography. As a matter of fact, we found that convective and non-convective precipitation amounts are both highly biased in all sensitivity simulations, so that the deep convective parameterization is not completely responsible for the overestimation of total precipitation.

Test runs using different parameterization schemes fail to determine a combination of schemes that performs well for both mountainous and plain areas. Low level zonal wind speed off the western U.S. coast are found to be 10%-15% higher in WRF than in CESM. With the topographic lifting of high mountains, more moisture brought by low level wind may lead to biases in both convective and non-convective precipitation.

Our collaborator Andrew Monaghan recently discovered a flaw in the preprocessing script where 4-D input variables like temperature and pressure from CESM are artificially perturbed to higher altitudes. Worse yet, the higher the altitude, the greater the deviation. As a result, WRF input fields have much warmer and wetter initial and boundary conditions at high altitudes. In this way, the atmosphere is not only warmer and wetter than CESM's, but also has an increased higher temperature and humidity gradient at lower levels where precipitation processes occur. This atmospheric profile provides too much humidity near surface and instability at lower levels. With the help of topographic lifting, humid air rises and condensates easily, thus producing much more precipitation than the original GCM.

New simulations with this problem fixed have been set up and are, at the time of writing, running. The new simulations contain several fix and upgrades. New code fixes errors over mountainous areas introduced when building WRF intermediate files. We also use WRF model version 3.6 instead of 3.3 in order to employ an updated version of the Kain-Fritsch convective parameterization that incorporates sub grid-scale cloud fraction and condensate feedbacks into the short wave and long wave radiation schemes (Herwehe et al., 2014). Correspondingly, the RRTM scheme is replaced by the RRTMG (Rapid Radiative Transfer Model-Global) to satisfy new convective scheme's requirement. Herwehe et al. (2014) has found that new Kain-Fritsch scheme helps to reduce excessive precipitation biases from WRF, especially over the northwestern U.S. The updated

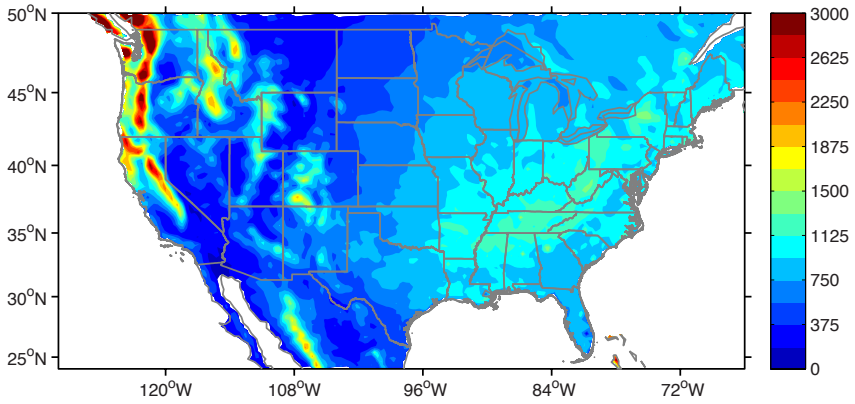

Figure 5.1: Mean annual precipitation (mm) from 1950-1960 from output of the upgraded version of historical downscaling simulation.

simulation has finished for the first decade of both the historical and the projected simulations. Maps of annual mean precipitation of the first decade (Fig. 5.1) clearly shows that the precipitation over mountainous areas have been improved relative to the original historical simulation, which greatly overstimated precipitation there. These new simulations will produce much more usable output over the western U.S. From Fig. 5.1, the annual mean precipitation has a similar spatial distribution to the annual mean precipitation of NARR over the contiguous U.S., although a slight dry bias still presents over southeastern U.S.

Our simulation results should be interpreted with the details of RCP6.0 scenario in mind. RCP6.0 specifies an increasing CO_2 global emission rate and the corresponding radiative forcing increasing rate that reach their peaks around 2080 and then start to decrease, unlike the continuously rising trend in RCP8.5 (Sanford et al., 2014; Meinshausen et al., 2011). But for the first half of 21st century, RCP6.0 still exhibits a rate of global temperature increase closer to RCP8.5 (Moss et al., 2010). Thus, this downscaling framework is possibly reproducing an accelerating global warming before 2080, and the weaker warming trend after that. For this reason, the increasing trend of TMAX extremes in the projected simulation is somewhat blunted compared to those in the historical simulation. Because of the nature of RCP6.0 scenario, performing an additional simulation for the first half of 21st century is critical. The new simulation will cover the entire period from 1950-2100, with the expectation of capturing continuous temporal trends of extremes over

that continuous period.

The stabilization of global CO_2 emission rate after 2080 in RCP6.0 scenario still results in more frequent heat waves with longer duration in the second half of 21st century, and our results suggest these increases result from not only the mean temperature increase, but also the more days with TMAX higher than mean TMAX. Together with the result that the frequency of extreme TMAX and TMIN increase/decrease more substantially than intensity, we found that the global mean temperature increase in the 21st century primarily leads to more extremely warm days and fewer cold nights, while the increase of TMAX and TMIN thresholds are close to the magnitude of mean temperature increase. The observation that the projected changes in TMAX and TMIN thresholds are so similar to the projected change in mean TMAX suggests that the change of the mean TMAX is more responsible for additional temperature extremes than are changes to the tail of the TMAX distribution.

Chapter 6

Conclusion and future work

This thesis uses dynamical downscaling to address the spatial distributions and temporal trends of the frequency and intensity of extreme events, as well as the occurrence of heat waves, over the contiguous United States. This dynamical downscaling framework performs better over the eastern U.S. than the western U.S., and better on the temperature field than the precipitation field. After bias-correction and omitting high-bias (> 40%) regions, precipitation and temperature fields are generally plausible.

Extreme thresholds of PR, TMAX, and TMIN are all found to increase in the projected simulation. Differences in PR threshold magnitudes between the projected and historical simulations increase with increasing percentiles (i.e., from PR differences from 90%, 95%, and 99% thresholds), whereas differences in TMAX and TMIN thresholds vary little with increasing percentiles. TMIN threshold increases comparing between the projected simulation and the historical simulation are greater than the TMAX threshold increases, which suggests a reduction of diurnal temperature variation in the projected simulation.

Trend maps for the precipitation extremes exhibit substantial spatial heterogeneity for both simulations, particularly for intensity, which depends more on small scale precipitation processes and how they are represented in WRF. Temperature extremes exhibit consistent warming trends in the historical simulation consistent with a warming climate, including increasing trend of TMAX

and decreasing trend of TMIN in both frequency and intensity. This trend is decelerated, however, in the projected simulation, especially for TMIN. We speculate that this decelerating trend at least partially results from the RCP6.0 scenario, in which the global CO_2 emission rate peaks around 2080 and decrease afterward, which ultimately slows warming in the model.

Statistics composited by Köppen-Geiger climate zones generally depict higher frequency and intensity in the projected simulation for all three variables in the projected simulation for all three variables (PR, TMAX, and TMIN). The increase in precipitation extremes varies substantially across different climate zones, and in the projected simulation precipitation intensity increases more than does frequency. This latter result is consistent with a similar number of heavy rain systems that each (on average) produce more precipitation. On the other hand, TMAX and TMIN have more consistent and significant differences, and the increase of TMAX extremes and decrease of TMIN extremes is better represented by changes in the frequency than intensity. This difference in behavior between precipitation and temperature extremes indicates the different causes of increasing extreme thresholds in the future. Precipitation thresholds increase by more local heavy rain processes, while increase of temperature extremes largely increase because of more warm events.

Heat waves are quantified in both WRF and CESM using the criteria of Meehl and Tebaldi (2004). Results indicate an increase in the duration and number of heat waves in the projected simulation. WRF and CESM show substantial agreement on these increases of frequencies and durations of heat waves. The heat wave increases are not only due to the daily mean temperature increase in the second half of 21^{st} century but also a higher percentage of TMAX days higher than mean TMAX. Projected TMAX under RCP6.0 scenario reproduces 3.5$\sim$4.5 heat waves with durations of 15$\sim$25 days on average each year, which is roughly 200% higher on the number of heat waves per year and 100% higher on duration relative to heat waves in the historical simulation.

Newly initialized historical and projected simulations have several fixes and updates compared to the first version. New software corrections fix the error when building initial 4-D fields for the WRF intermediate files. The latest version of WRF involves upgraded Kain-Fristch scheme with radiation feedbacks. Modeling entire 150-year period from 1950 to 2100 will help uncover the ex-

treme behavior in the first half of 21st century, which is critical for fully understanding the behavior of RCP6.0 scenario that includes decreasing trend of CO_2 emission rate after 2080. Mean annual precipitation map of the first decade of the new historical simulation indicates greatly improved mean precipitation pattern over the contiguous United States. With these model improvements, future work will be able to include analysis on historical and projected ENSO teleconnections to extreme precipitation and temperature events.

References

Alexander, L., et al., 2006: Global observed changes in daily climate extremes of temperature and precipitation. *J. geophys. Res*, **111 (D05109)**, 22.

Becker, E. J., E. H. Berbery, and R. W. Higgins, 2009: Understanding the characteristics of daily precipitation over the united states using the north american regional reanalysis. *Journal of Climate*, **22 (23)**.

Bell, J. L., L. C. Sloan, and M. A. Snyder, 2004: Regional changes in extreme climatic events: A future climate scenario. *Journal of Climate*, **17**, 81–87.

Betts, A. and M. Miller, 1986: A new convective adjustment scheme. part ii: Single column tests using gate wave, bomex, atex and arctic air-mass data sets. *Quarterly Journal of the Royal Meteorological Society*, **112 (473)**, 693–709.

Betts, A. K., 1986: A new convective adjustment scheme. part i: Observational and theoretical basis. *Quarterly Journal of the Royal Meteorological Society*, **112 (473)**, 677–691.

Bukovsky, M. S., D. J. Gochis, and L. O. Mearns, 2013: Towards assessing narccap regional climate model credibility for the north american monsoon: Current climate simulations*. *Journal of Climate*, **26 (22)**, 8802–8826.

Bukovsky, M. S. and D. J. Karoly, 2007: A brief evaluation of precipitation from the north american regional reanalysis. *Journal of Hydrometeorology*, **8 (4)**.

Bukovsky, M. S. and D. J. Karoly, 2009: Precipitation simulations using wrf as a nested regional climate model. *Journal of Applied Meteorology and Climatology*, **48 (10)**, 2152–2159.

Caldwell, P., H.-N. S. Chin, D. C. Bader, and G. Bala, 2009: Evaluation of a wrf dynamical downscaling simulation over california. *Climatic Change*, **95 (3-4)**, 499–521.

Dudhia, J., 1996: A multi-layer soil temperature model for mm5. *Preprints, The Sixth PSU/NCAR mesoscale model users' workshop*, 22–24.

Duffy, P., et al., 2006: Simulations of present and future climates in the western united states with four nested regional climate models. *Journal of Climate*, **19 (6)**, 873–895.

Easterling, D. R., J. L. Evans, P. Y. Groisman, T. R. Karl, K. E. Kunkel, and P. Ambenje, 2000a: Observed variability and trends in extreme climate events: A brief review*. *Bulletin of the American Meteorological Society*, **81 (3)**, 417–425.

Easterling, D. R., G. A. Meehl, C. Parmesan, S. A. Changnon, T. R. Karl, and L. O. Mearns, 2000b: Climate extremes: observations, modeling, and impacts. *science*, **289 (5487)**, 2068–2074.

Gent, P. R., et al., 2011: The community climate system model version 4. *Journal of Climate*, **24 (19)**, 4973–4991.

Groisman, P. Y., R. W. Knight, and T. R. Karl, 2001: Heavy precipitation and high streamflow in the contiguous united states: Trends in the twentieth century. *Bulletin of the American Meteorological Society*, **82 (2)**, 219–246.

Gutowski, W., et al., 2010: Regional extreme monthly precipitation simulated by narccap rcms. *Journal of Hydrometeorology*, **11 (6)**, 1373–1379.

Herwehe, J. A., K. Alapaty, T. L. Spero, and C. G. Nolte, 2014: Increasing the credibility of regional climate simulations by introducing subgrid-scale cloud-radiation interactions. *Journal of Geophysical Research: Atmospheres*, **119 (9)**, 5317–5330.

Higgins, R. W., V. E. Kousky, and P. Xie, 2011: Extreme precipitation events in the south-central united states during may and june 2010: Historical perspective, role of enso, and trends. *Journal of Hydrometeorology*, **12 (5)**, 1056–1070.

Hong, S.-Y. and J. Dudhia, 2003: 17.3 testing of a new nonlocal boundary layer vertical diffusion scheme in numerical weather prediction applications.

Janjic, Z. I., 1994: The step-mountain eta coordinate model: Further developments of the convection, viscous sublayer, and turbulence closure schemes. *Monthly Weather Review*, **122 (5)**, 927–945.

Kain, J. S., 2004: The kain–fritsch convective parameterization: an update. *Journal of Applied Meteorology*, **43 (1)**.

Kottek, M., J. Grieser, C. Beck, B. Rudolf, and F. Rubel, 2006: World map of the koppen-geiger climate classification updated. *Meteorologische Zeitschrift*, **15 (3)**, 259–263.

Kunkel, K., D. Easterling, K. Redmond, and K. Hubbard, 2003: Temporal variations of extreme precipitation events in the united states: 1895–2000. *Geophysical Research Letters*, **30 (17)**, 1900.

Lenderink, G., A. Buishand, and W. v. Deursen, 2007: Estimates of future discharges of the river rhine using two scenario methodologies: direct versus delta approach. *Hydrology and Earth System Sciences*, **11 (3)**, 1145–1159.

Maraun, D., et al., 2010: Precipitation downscaling under climate change: Recent developments to bridge the gap between dynamical models and the end user. *Reviews of Geophysics*, **48 (3)**.

Mearns, L. O., et al., 2012a: The north american regional climate change assessment program: overview of phase i results. *Bulletin of the American Meteorological Society*, **93 (9)**, 1337–1362.

Mearns, L. O., et al., 2012b: The north american regional climate change assessment program. *Bulletin of the American Meteorological Society*, **93 (9)**.

Meehl, G. A. and C. Tebaldi, 2004: More intense, more frequent, and longer lasting heat waves in the 21st century. *Science*, **305 (5686)**, 994–997.

Meinshausen, M., et al., 2011: The rcp greenhouse gas concentrations and their extensions from 1765 to 2300. *Climatic change*, **109 (1-2)**, 213–241.

Mesinger, F., et al., 2006: North american regional reanalysis. *Bulletin of the American Meteorological Society*, **87 (3)**, 343–360.

Mlawer, E. J., S. J. Taubman, P. D. Brown, M. J. Iacono, and S. A. Clough, 1997: Radiative transfer for inhomogeneous atmospheres: Rrtm, a validated correlated-k model for the longwave. *Journal of Geophysical Research: Atmospheres (1984–2012)*, **102 (D14)**, 16 663–16 682.

Moss, R. H., et al., 2010: The next generation of scenarios for climate change research and assessment. *Nature*, **463 (7282)**, 747–756.

Nakicenovic, N., et al., 2000: Emissions scenarios.

Noilhan, J. and S. Planton, 1989: A simple parameterization of land surface processes for meteorological models. *Monthly Weather Review*, **117 (3)**, 536–549.

Parmesan, C., T. L. Root, and M. R. Willig, 2000: Impacts of extreme weather and climate on terrestrial biota*. *Bulletin of the American Meteorological Society*, **81 (3)**, 443–450.

Peterson, T. C., et al., 2013: Monitoring and understanding changes in heat waves, cold waves, floods, and droughts in the united states: state of knowledge. *Bulletin of the American Meteorological Society*, **94 (6)**, 821–834.

Sanford, T., P. C. Frumhoff, A. Luers, and J. Gulledge, 2014: The climate policy narrative for a dangerously warming world. *Nature Climate Change*, **4 (3)**, 164–166.

Skamarock, W., J. Klemp, J. Dudhia, D. Gill, D. Barker, W. Wang, and J. Powers, 2005: A description of the advanced research wrf version 2. Tech. rep., DTIC Document.

Solomon, S., D. Qin, M. Manning, Z. Chen, M. Marquis, K. Averyt, M. Tignor, and H. Miller, 2007: Contribution of working group i to the fourth assessment report of the intergovernmental panel on climate change, 2007.

Taylor, K. E., R. J. Stouffer, and G. A. Meehl, 2012: An overview of cmip5 and the experiment design. *Bulletin of the American Meteorological Society*, **93 (4)**.

Teutschbein, C. and J. Seibert, 2012: Bias correction of regional climate model simulations for hydrological climate-change impact studies: Review and evaluation of different methods. *Journal of Hydrology*, **456**, 12–29.

Weller, G. B., D. Cooley, S. R. Sain, M. S. Bukovsky, and L. O. Mearns, 2013: Two case studies on narccap precipitation extremes. *Journal of Geophysical Research: Atmospheres*, **118 (18)**, 10,475–10,489, doi:10.1002/jgrd.50824, URL `http://dx.doi.org/10.1002/jgrd.50824`.

Wilson, C. J., N. Brunsell, C. Young, L. Miller, and D. Mechem, 2014: Trends in 20^{th} century weather extremes over the contiguous united states. *Journal of climate, in review*.

Wuebbles, D., et al., 2014: Cmip5 climate model analyses: climate extremes in the united states. *Bulletin of the American Meteorological Society*.